Supporting Information

General Synthetic Route Towards Highly Dispersed Metal Clusters Enabled by Poly(ionic liquid)s

Jian-Ke Sun, Zdravko Kochovski, Wei-Yi Zhang, Holm Kirmse, Yan Lu, Markus Antonietti, and Jiayin Yuan*

1. Chemicals and Instrumentation

All chemicals were from commercial sources and used without further purification.

Transmission electron microscopy (TEM) was performed on a JEOL 2010FS transmission electron microscope operated at 120 kV. Scanning transmission electron microscopy (STEM) was performed on a Jeol JEM-2200FS transmission electron microscope operated at 200 kV equipped with a high-angle annular dark-field (HAADF) STEM detector. Cryogenic transmission electron microscopy (cryo-EM) was performed with a JEOL JEM-2100 transmission electron microscope (JEOL GmbH, Eching, Germany). Cryo-EM specimens were prepared by applying a 4 µl drop of a dispersion sample to holey carbon-coated copper TEM grids (Quantifoil Micro Tools GmbH, Jena, Germany) and plunge-frozen into liquid ethane with an FEI vitrobot Mark IV set at 4°C and 95% humidity. Vitrified grids were either transferred directly to the microscope cryo transfer holder (Gatan 914, Gatan, Munich, Germany) or stored in liquid nitrogen. Imaging was carried out at temperatures around 90 K. The TEM was operated at an acceleration voltage of 200 kV, and a defocus of the objective lens of about 3.5 − 4 µm was used to increase the contrast. Cryo-EM micrographs were recorded at a number of magnifications with a bottom-mounted 4*4k CMOS camera (TemCam-F416, TVIPS, Gauting, Germany). The total electron dose in each micrograph was kept below 20 $e^-/Å^2$. Powder X-ray diffraction (PXRD) was carried out on an X-ray diffractometer of Rigaku, Ultima IV. X-ray photoelectron spectroscopy (XPS) studies were performed on a ThermoFisher ESCALAB250 X-ray photoelectron spectrometer (powered at 150 W) using Al K_α radiation (λ = 8.357 Å). To compensate for surface charging effects, all XPS spectra were referenced to the C 1s neutral carbon peak at 284.6 eV. The solution UV-Vis absorption measurements were recorded on a Lambda 900 spectrophotometer. ^{1}H and

^{13}C nuclear magnetic resonance (^{1}H-NMR) measurements were carried out at room temperature on a Bruker DPX-400 spectrometer in different deuterated solvents. The energy-dispersive X-ray (EDX) mapping measurements were taken on a Gemini scanning electron microscope (SEM) with an EDX spectrometer. Thermogravimetric analysis (TGA) experiments were carried out by a Netzsch TG209-F1 apparatus at a heating rate of 10 K min^{-1} under a constant N_2 flow. Differential scanning calorimetry (DSC) measurements were conducted on a Perkin-Elmer DSC-1 instrument at a heating rate of 10 K min^{-1} under a N_2 flow.

2. Experimental Section

2.1 Synthesis of poly(ionic liquid)s

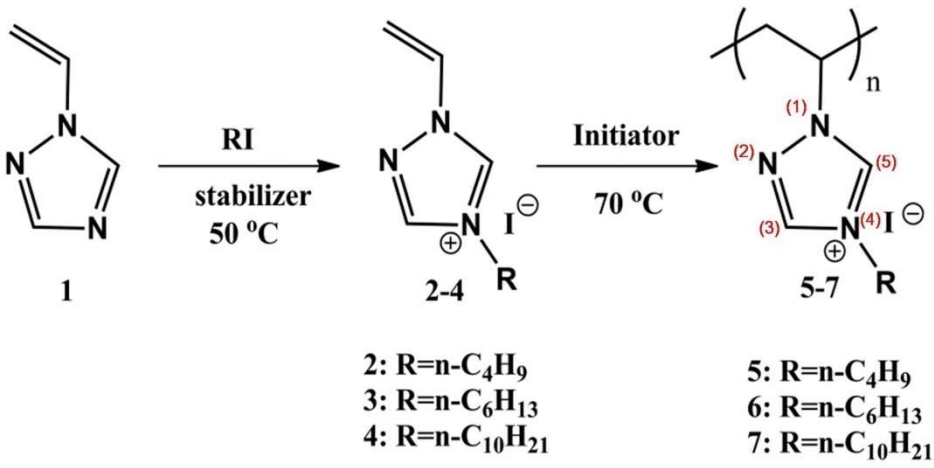

Scheme S1. Synthetic procedure of triazolium poly(ionic liquid)s with different alkyl chain length.

Polymer 5: Poly(4-butyl-1-vinyl-1,2,4-triazolium iodide) (simplified as "PIL-butyl"), the positions of atoms in the triazolium ring are highlighted in red color (similarly hereinafter).

Polymer 6: Poly(4-hexyl-1-vinyl-1,2,4-triazolium iodide) (simplified as "P(triaz)")

Polymer 7: Poly(4-decyl-1-vinyl-1,2,4-triazolium iodide) (simplified as "PIL-decyl")

Monomer 2-4 synthesis: A mixture of 1-vinyl-1,2,4-triazole **1** (5 mL, 5.5g, 57.83 mmol) and a 1.2 equivalent amount of n-iodoalkanes (1-iodobutane, 1-iodohexane and 1-iododecane) were added into a 100 mL round flask, accompanied with 2,6-di-tert-butyl-4-methylphenol (50 mg, 0.227 mol) as the stabilizer. After heated at 50 °C overnight, crude products were precipitated in diethyl ether and washed with the same solvent for three times. Pale yellow powders were obtained after purification.

Polymer 5-7 synthesis: A mixture of monomers (**2-4**) with AIBN (1.5 mol%) as initiator was added to anhydrous DMF (concentration: ~1 g monomer in 10 mL solvent) inside a 100 mL round-bottom schlenk flask. The flask was treated with three freeze-pump-thaw cycles and finally purged with argon. The reaction was stirred at 70 °C for 24 h under argon atmosphere. Yellow powders were obtained after dialysis against water and a vacuum drying process.

The preparation methods of 4-hexyl-1-vinyl-imidazolium iodide and poly(4-hexyl-1-vinyl-imidazolium iodide) (simplified as "PIL-imidaz") were described in the literature [Salamone, J. C.; Israel, S. C.; Taylor, P.; Snider, B., Synthesis and homopolymerization studies of vinylimidazolium salts. *Polymer,* 1973, *14*, 639-644.]

The chemical structures of the polymers used in the present work were confirmed by ^{1}H NMR spectra in Figure S1-4.

4-Butyl-1-vinyl-1,2,4-triazolium iodide (**2**) (Yield: 92%, 14.84 g): ^{1}H NMR (400 MHz, DMSO-d_6, δ, ppm): 10.55 (s, 1H), 9.45 (s, 1H), 7.50 (dd, 1H, J_1=16 Hz, J_2=8 Hz), 6.03 (d, 1H, J=16 Hz), 5.58 (d, 1H, J=8 Hz), 4.32 (t, 2H, J=8 Hz), 1.86 (m, 2H), 1.32 (m, 2H), 0.88 (t, 3H, J=8 Hz); ^{13}C NMR (400 MHz, DMSO-d_6, δ, ppm): 145.25, 142.14, 129.75, 110.79, 48.18, 30.09, 19.27, 13.81.

4-Hexyl-1-vinyl-1,2,4-triazolium iodide (**3**) (Yield: 96%, 17.04 g): ^{1}H NMR (400 MHz, DMSO-d_6, δ, ppm): 10.55 (s, 1H), 9.45 (s, 1H), 7.51 (dd, 1H, J_1=16 Hz, J_2=8 Hz), 6.04 (d, 1H, J=16 Hz), 5.58 (d, 1H, J=8 Hz), 4.31 (t, 2H, J=8 Hz), 1.88 (m, 2H), 1.26 (m, 6H), 0.83 (t, 3H,

J=8 Hz); ^{13}C NMR (400 MHz, DMSO-d_6, δ, ppm): 145.25, 142.15, 129.76, 110.72, 48.41, 31.00, 28.94, 25.58, 22.29, 14.31.

4-Decyl-1-vinyl-1,2,4-triazolium iodide (**4**) (Yield: 95%, 19.94 g): ^{1}H NMR (400 MHz, DMSO-d_6, δ, ppm): 10.46 (s, 1H), 9.40 (s, 1H), 7.52 (dd, 1H, J_1=16 Hz, J_2=8 Hz), 6.05 (d, 1H, *J*=16 Hz), 5.58 (d, 1H, *J*=8 Hz), 4.29 (t, 2H, *J*=8 Hz), 1.87 (m, 2H), 1.28 (m, 14H), 0.84 (t, 3H, *J*=8 Hz); ^{13}C NMR (400 MHz, DMSO-d_6, δ, ppm): 145.30, 142.19, 129.77, 110.64, 48.36, 31.74, 29.36, 29.24, 29.14, 29.03, 28.86, 25.93, 22.55, 14.41.

Poly(4-butyl-1-vinyl-1,2,4-triazolium iodide) (PIL-butyl-C4) (**5**) (Yield: 82%, 3.24 g): ^{1}H NMR (400 MHz, DMSO-d_6, δ, ppm): 10.53 (br, 1H), 9.34 (m, 1H), 4.67 (m, 1H), 4.26 (br, 2H), 2.52 (br, 2H), 1.91 (br, 2H), 1.38 (m, 2H), 0.94 (br, 3H).

Poly(4-hexyl-1-vinyl-1,2,4-triazolium iodide) (P(triaz)) (**6**) (Yield: 76%, 2.78 g): ^{1}H NMR (400 MHz, DMSO-d_6, δ, ppm): 10.51 (br, 1H), 9.33 (m, 1H), 4.75 (m, 1H), 4.23 (br, 2H), 2.58 (br, 2H), 1.90 (br, 2H), 1.30 (br, 6H), 0.85 (br, 3H).

Poly(4-decyl-1-vinyl-1,2,4-triazolium iodide) (PIL-decyl) (7) (Yield: 68%, 2.51 g): ^{1}H NMR (400 MHz, DMSO-d_6, δ, ppm): 10.68 (br, 1H), 8.92 (br, 1H), 5.23 (m, 1H), 4.28 (br, 2H), 2.71 (br, 2H), 2.01 (br, 2H), 1.20 (br, 14H), 0.82 (br, 3H).

2.2 Analytical Ultracentrifugation (AUC): The weight-averaged molecular weight of P(triaz) and PIL-imidaz polymers were analyzed by AUC method. The sample was dissolved in ethanol with 0.5M NaI to avoid charge effects in the analysis. The partial specific volume of the samples was determined in a density oscillation tube (DMA 5000, Anton Paar, Graz) (0.673 ml/g for PIL-imidaz and 0.596 ml/g for P(triaz)) Equilibrium experiments have been performed on an Optima XLI ultracentrifuge (Beckman Coulter, Palo Alto) and interference optics. Seven concentrations have been analyzed at different speeds starting from 7500 rpm up to 30000 rpm. Data were evaluated with the program MSTAR (Kristian Schilling, Nanolytics, Germany).

2.3 Synthesis of metal cluster (MC) stabilized by PILs

Synthesis of Pd/P(triaz). In a typical synthesis, 9 mL of dichloromethane and methanol mixture (volume ratio = 2:1) containing 5 mg of P(triaz) was subsequently added to 0.5 mL of methanol containing $Pd(NO_3)_2 \cdot 2H_2O$ (0.5 mg Pd in content). The resultant mixture solution was further homogenized after aging for 20 min. Then, 0.5 mL of methanol solution containing 5 mg of $NaBH_4$ was immediately added into the above solution with vigorous shaking, resulting in a well transparent dispersion of Pd/P(triaz).

Synthesis of other MCs stabilized by P(triaz). The synthetic procedure used above to prepare Pd/P(triaz) was followed by using 0.5 mL of methanol containing $AgNO_3$, H_2PtCl_4, $HAuCl_4 \cdot 3H_2O$, $RuCl_3 \cdot 3H_2O$, $Rh(OAc)_3$, $Ni(NO_3)_2 \cdot 6H_2O$, $Co(NO_3)_2 \cdot 6H_2O$, or $Cu(NO_3)_2 \cdot 2.5H_2O$ (The metal in content is 0. 5 mg except for Ru, in which 1 mg metal was included) in place of $Pd(NO_3)_2 \cdot 2H_2O$.

Synthesis of Pd/PIL-imidaz. The synthetic procedure used above to prepare Pd/P(triaz) was followed by using 9 mL of dichloromethane and methanol mixture (volume ratio = 2:1) containing poly(3-hexyl-1-vinylimidazolium iodide) (PIL-imidaz) (5 mg) in place of P(triaz).

Synthesis of Pd/triazolium monomer. The synthetic procedure used above to prepare Pd/P(triaz) was followed by using 9 mL of dichloromethane and methanol mixture (volume ratio = 2:1) containing triazolium monomer (5 mg) in place of P(triaz).

Synthesis of Ag/P(triaz) by UV reduction (instead of $NaBH_4$ reduction). 9 mL of dichloromethane and methanol mixture (volume ratio = 2:1) containing 5 mg of P(triaz) was subsequently added to 0.5 mL of methanol containing $AgNO_3$ (0.5 mg Ag in content). The

resultant mixture was further homogenized after aging for 20 min. Then, solution was irradiated with UV light (125 mW cm^{-2}) for 6 h, resulting in Ag/P(triaz) nanoparticle.

2.4 Synthesis of catalyst for AB methanolysis reaction

Synthesis of Rh/P(triaz) catalyst. The synthetic procedure used above to prepare Pd/P(triaz) was followed by using 9 mL of dichloromethane and methanol mixture (volume ratio = 2:1) containing P(triaz) (2.5 mg), 0.5 mL of methanol containing $Rh(OAc)_3$, (1 mg Rh in content) in place of $Pd(NO_3)_2 \cdot 2H_2O$.

Synthesis of Rh/P(triaz) catalyst in pure methanol. The synthetic procedure used above to prepare Rh/P(triaz) catalyst was followed by using 9 mL of methanol .

Synthesis of Rh-P(triaz)-Free catalyst. The synthetic procedure used above to prepare Rh/P(triaz) catalyst was followed by using 9 mL of dichloromethane and methanol mixture (volume ratio = 2:1) without P(triaz) as stabilizer.

Synthesis of Rh/PIL-butyl catalyst. The synthetic procedure used above to prepare Rh/P(triaz) catalyst was followed by using 9 mL of dichloromethane and methanol mixture (volume ratio = 2:1) containing the PIL-butyl (2.5 mg) in place of P(triaz).

Synthesis of Rh-triazolium monomer catalyst. The synthetic procedure used above to prepare Rh/P(triaz) catalyst was followed by using 9 mL of dichloromethane and methanol mixture (volume ratio = 2:1) containing the triazolium monomer (2.5 mg) in place of P(triaz).

Synthesis of Ru/PAMAM-OH catalyst. The synthetic procedure used above to prepare Rh/P(triaz) catalyst was followed by using 9 mL of dichloromethane and methanol mixture (volume ratio = 2:1) containing PAMAM-OH (2.5 mg) in place of P(triaz).

2.5 Catalytic activity characterization

Procedure for the methanolysis of AB by Rh/P(triaz) catalyst: The reaction apparatus for measuring the hydrogen evolution from the methanolysis of AB is as follows. In general, the as-synthesized Rh/P(triaz) catalyst was placed in a two-necked round-bottomed flask (30 mL), which was placed in a water bath under ambient atmosphere. A gas burette filled with water was connected to the reaction flask to measure the volume of hydrogen. The reaction started when AB (30.8 mg) in 0.8 mL methanol was added into the flask. The volume of the evolved hydrogen gas was monitored by recording the displacement of water in the gas burette. The reaction was completed when there was no more gas generation. The methanolysis of AB can be expressed as follows:

$$NH_3BH_3 + 4CH_3OH \rightarrow NH_4B(CH_3O)_4 + 3H_2 \quad (1)$$

Procedures for the methanolysis of AB by Rh/P(triaz)-methanol, Rh/PIL-butyl, Rh-SP-Free, Rh-triazolium monomer catalyst and Ru/PAMAM-OH catalysts: The procedures for the methanolysis of AB were similar to that of Rh/P(triaz) catalyst except different catalysts were used.

Procedures for the methanolysis of AB by redissolving N_2 atmosphere dried Rh/P(triaz) powder in solvents. The as-synthesized Rh/P(triaz) solution was first dried in N_2 atmosphere, which was further washed by water and dried in vacuum oven. The resultant powder was re-dissolved in 9 mL of dichloromethane and methanol mixture (2:1) to generate the solution catalysts for catalytic reaction.

3. Additional data and figures

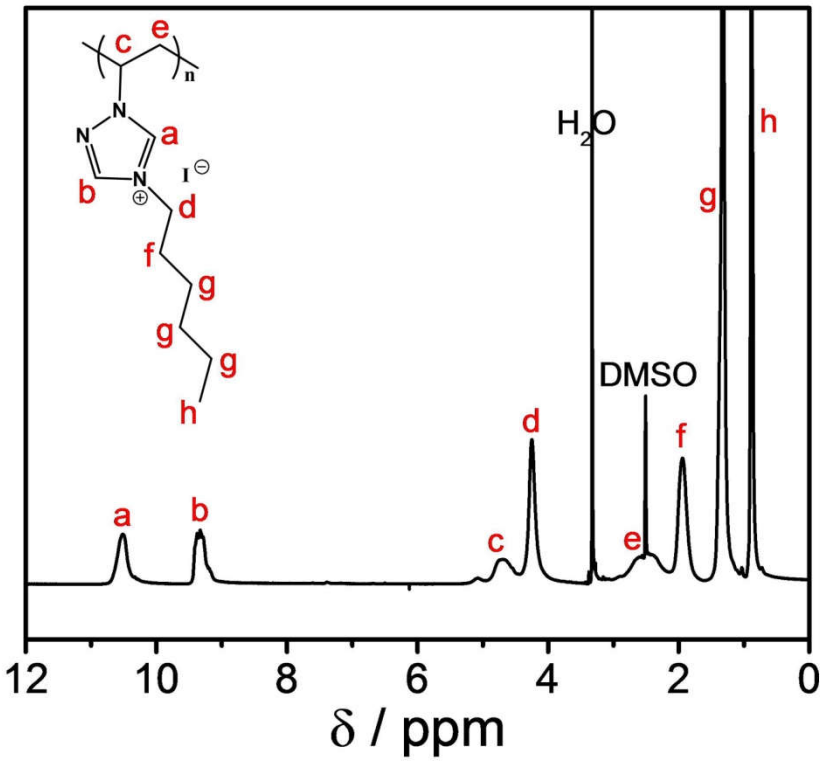

Figure S1. Chemical structure and ^{1}H-NMR spectrum of poly(4-hexyl-1-vinyl-1,2,4-triazolium iodide) (P(triaz)).

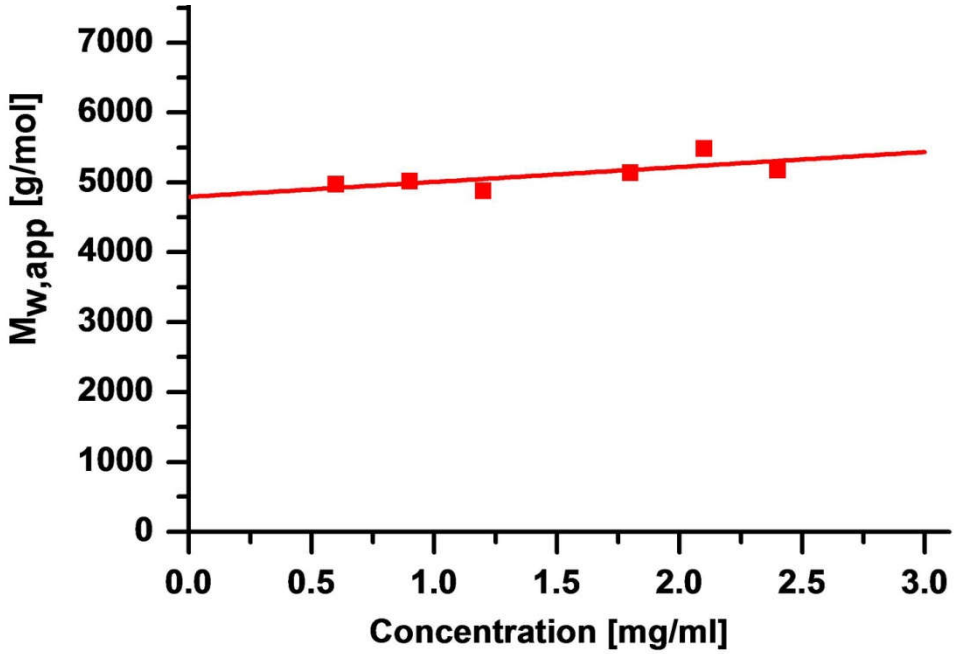

Figure S2. AUC analysis of P(triaz). The absolute weight-averaged molecular weight M_w is determined to be 4.8x10^3 g mol^{-1}.

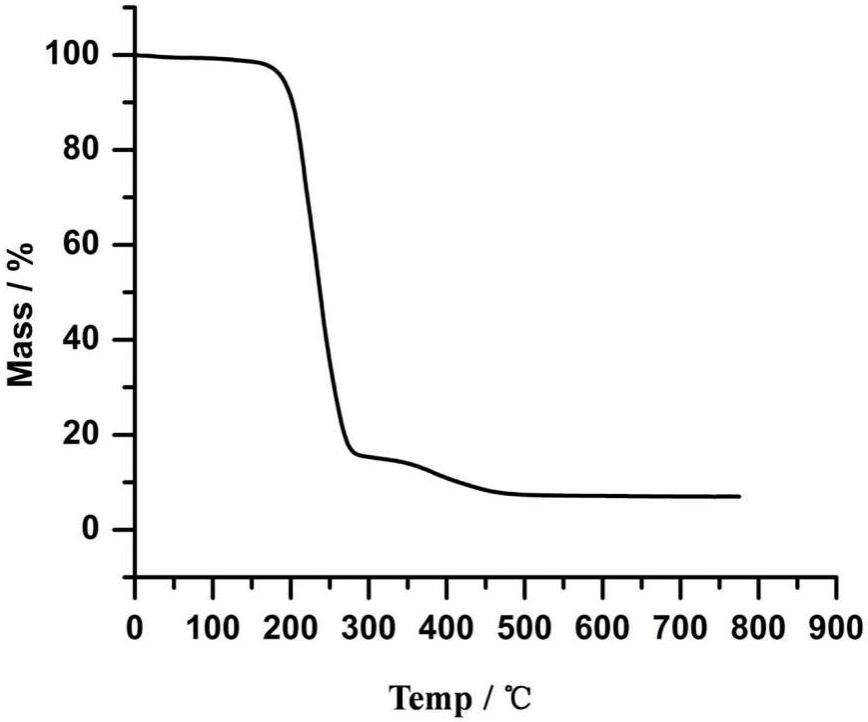

Figure S3. TGA plot of P(triaz) under N_2.

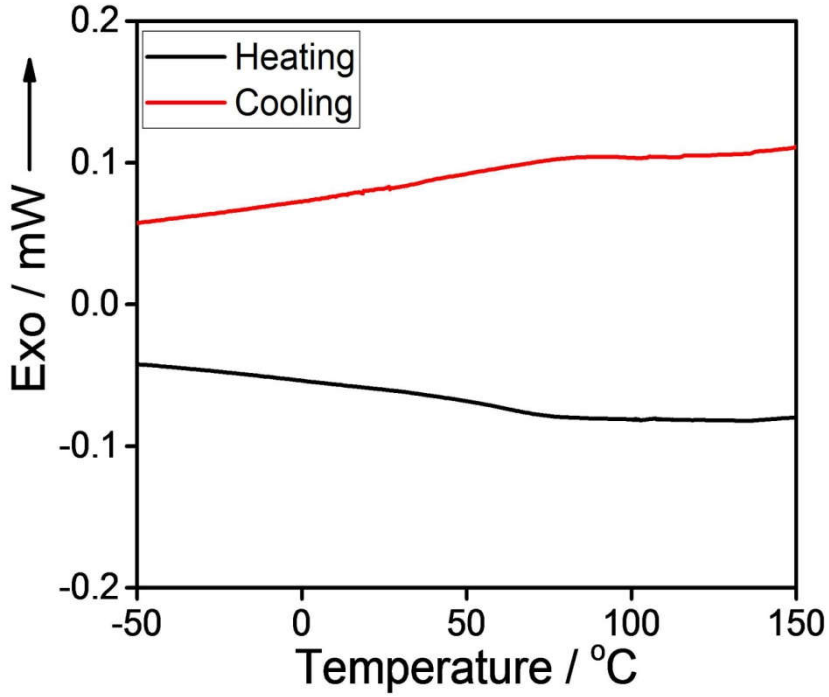

Figure S4. The DSC plot of P(triaz).

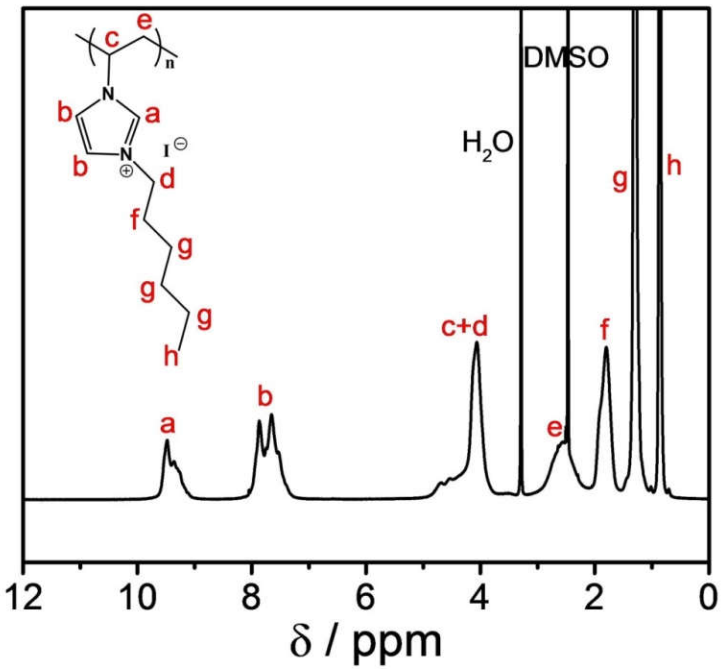

Figure S5. Chemical structure and ^{1}H-NMR spectrum of poly(4-hexyl-1-vinyl-imidazolium iodide) (PIL-imidaz).

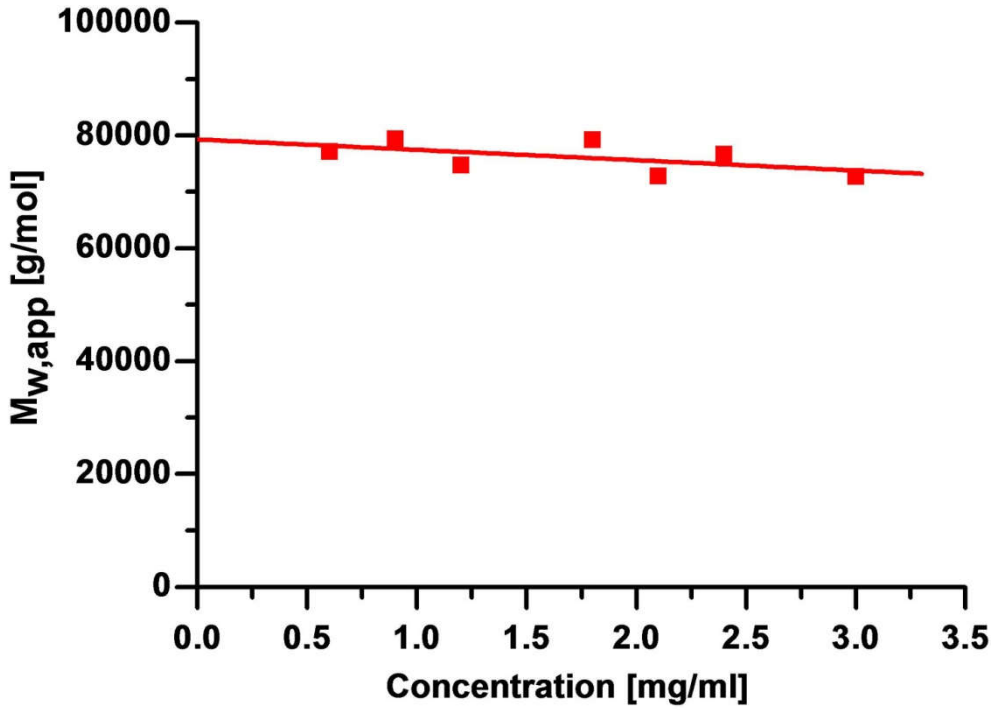

Figure S6. AUC analysis of PIL-imidaz. The absolute weight-averaged molecular weight M_w is determined to be 7.9x10^4 g mol^{-1}.

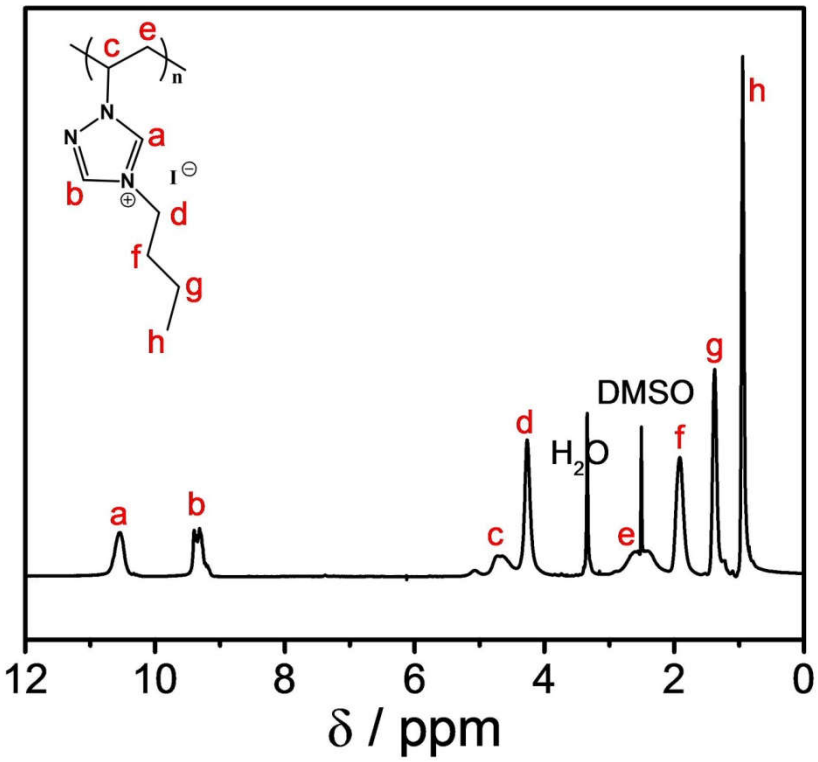

Figure S7. Chemical structure and ^{1}H-NMR spectrum of poly(4-butyl -1-vinyl-1,2,4-triazolium iodide) (PIL-butyl).

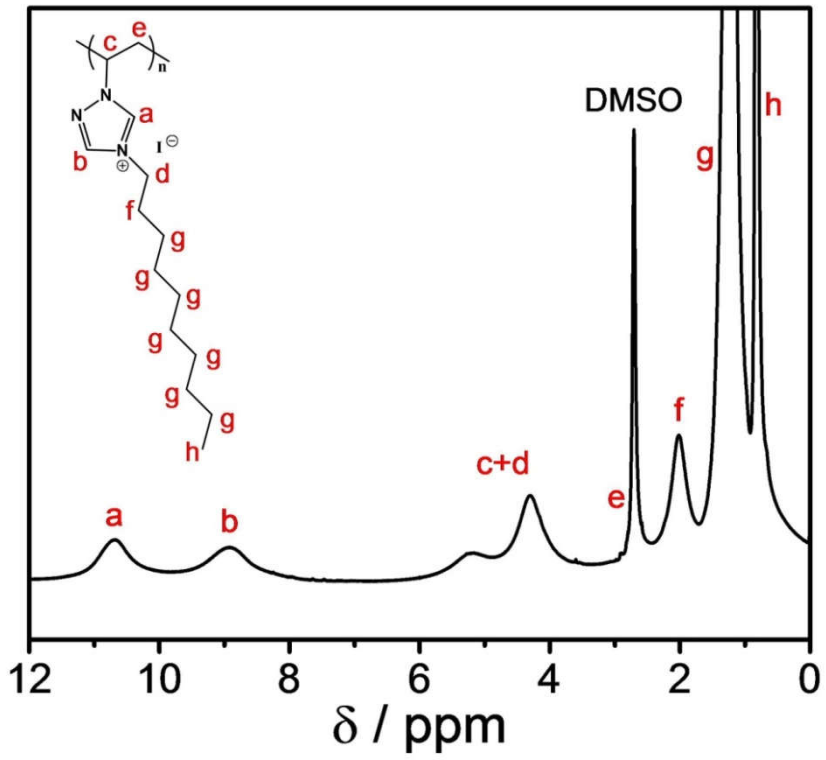

Figure S8. Chemical structure and ^{1}H-NMR spectrum of poly(4-decyl -1-vinyl-1,2,4-triazolium iodide) (PIL-decyl).

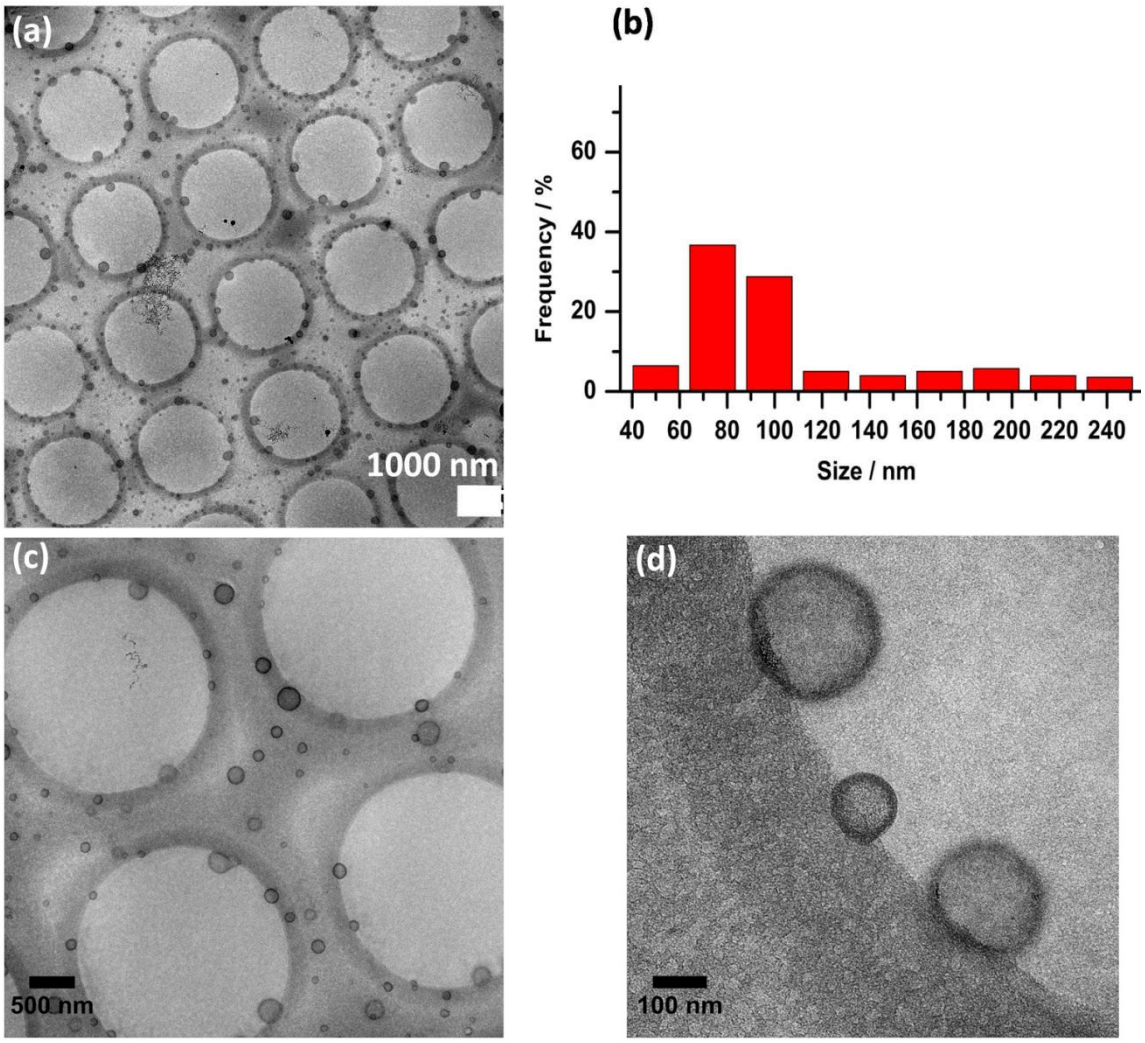

Figure S9. (a) A cryo-EM image of a low magnification of the vesicular P(triaz) in dichloromethane and methanol mixture (volume ratio = 2:1). Note, the bright large circles are from the Quantifoil carbon grid. (b) The corresponding size distribution histogram. (c-d) Cryo-EM images of vesicles at different magnifications.

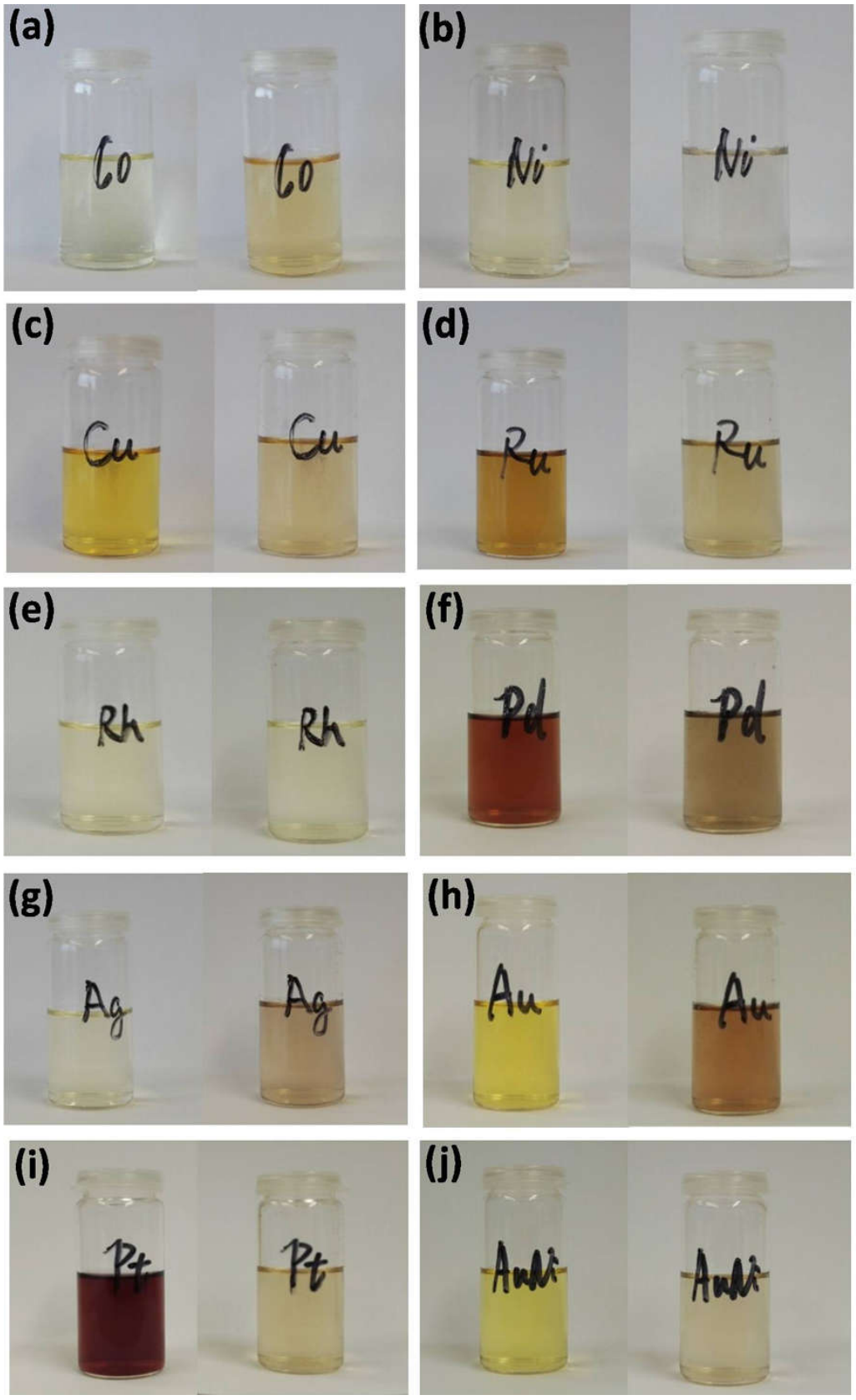

Figure S10. Photographs illustrating the synthesis of MC/P(triaz). The corresponding metal ion/P(triaz) (left) and MC/P(triaz) (right) in a dichloromethane and methanol mixture (volume ratio = 2:1) were shown in each photograph.

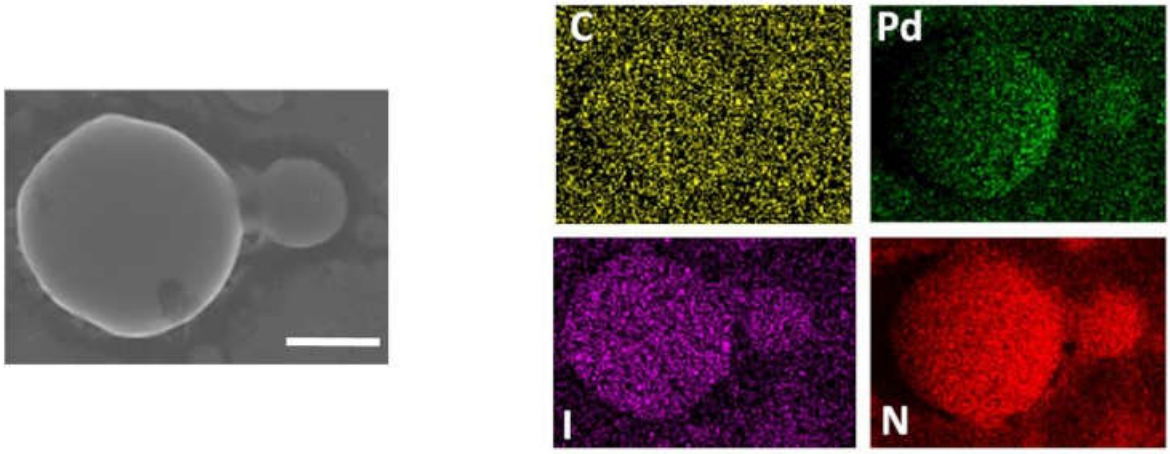

Figure S11. Left: a SEM image of a dried Pd/P(triaz) sample, scale bar: 5 μm (note that they are not the individual polymer vesicles but their aggregates due to the drying process). Right: The C, Pd, I and N elemental mapping of the same Pd/P(triaz) sample.

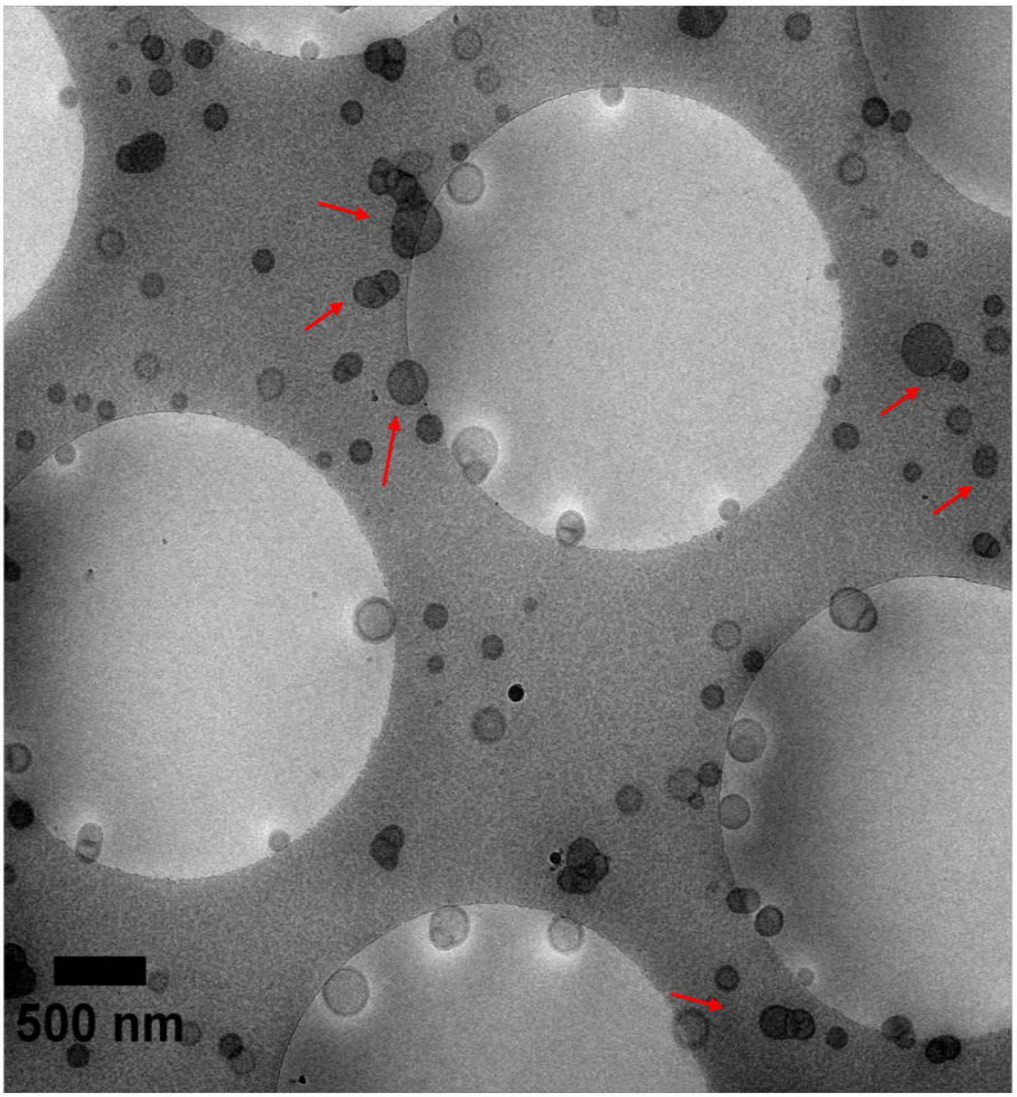

Figure S12. The cryo-EM image of the Pd/P(triaz) hybrid vesicles at a low magnification. Red arrows highlight the dark shell of the vesicles.

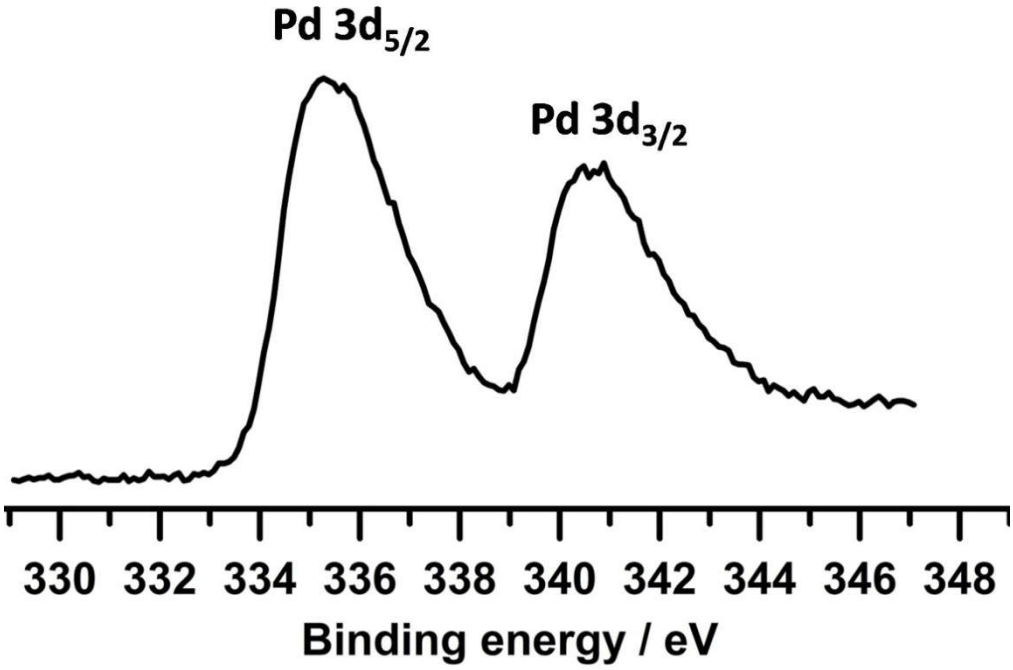

Figure S13. XPS spectrum of Pd/P(triaz) showing Pd $3d_{5/2}$ (335.3 eV) and $3d_{3/2}$ (340.6 eV) peaks of metallic Pd after Ar etching.

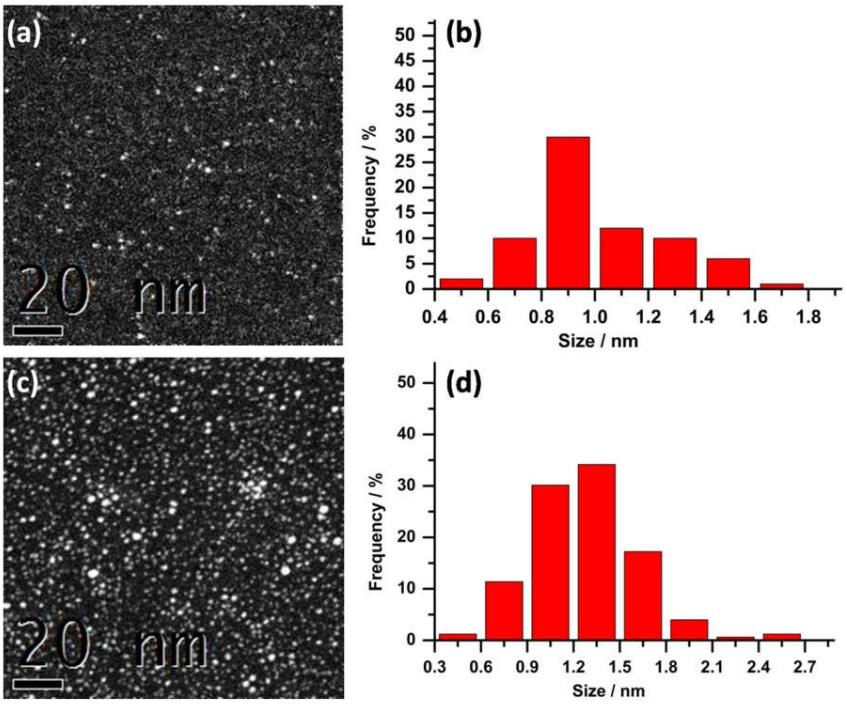

Figure S14. (a) HAADF-STEM image and (b) the corresponding size distribution histogram of Pd (4.8 wt%) clusters (size: 1.0 ± 0.2 nm). (c) HAADF-STEM image and (d) the corresponding size distribution histogram of Pd (14.5 wt%) clusters (size: 1.2 ± 0.3 nm).

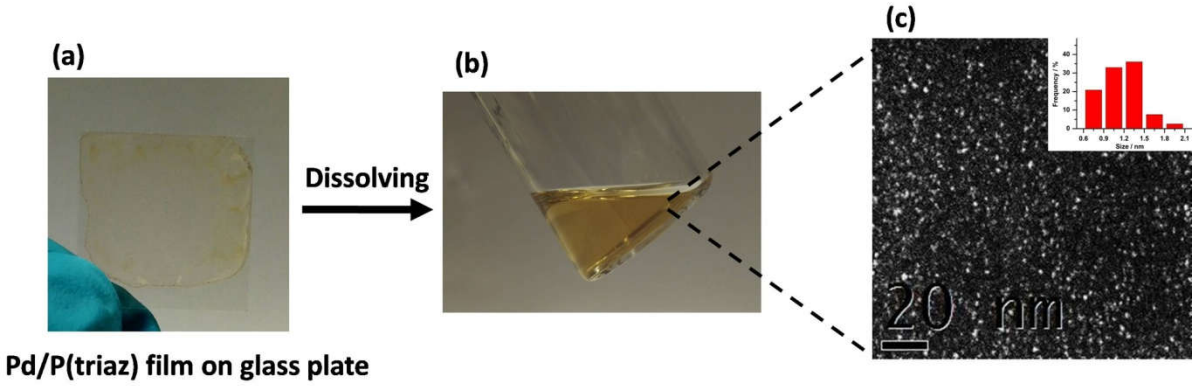

Figure S15. The illustration of the excellent processability of Pd/P(triaz) in a solution state. (a) The drop-casting of Pd/P(triaz) onto a piece of glass plate. (b) The film can re-dissolve in dichloromethane and methanol mixture (volume ratio = 2:1). (c) The HAADF-STEM image and the corresponding size distribution histogram (inset) of the redispersed Pd clusters.

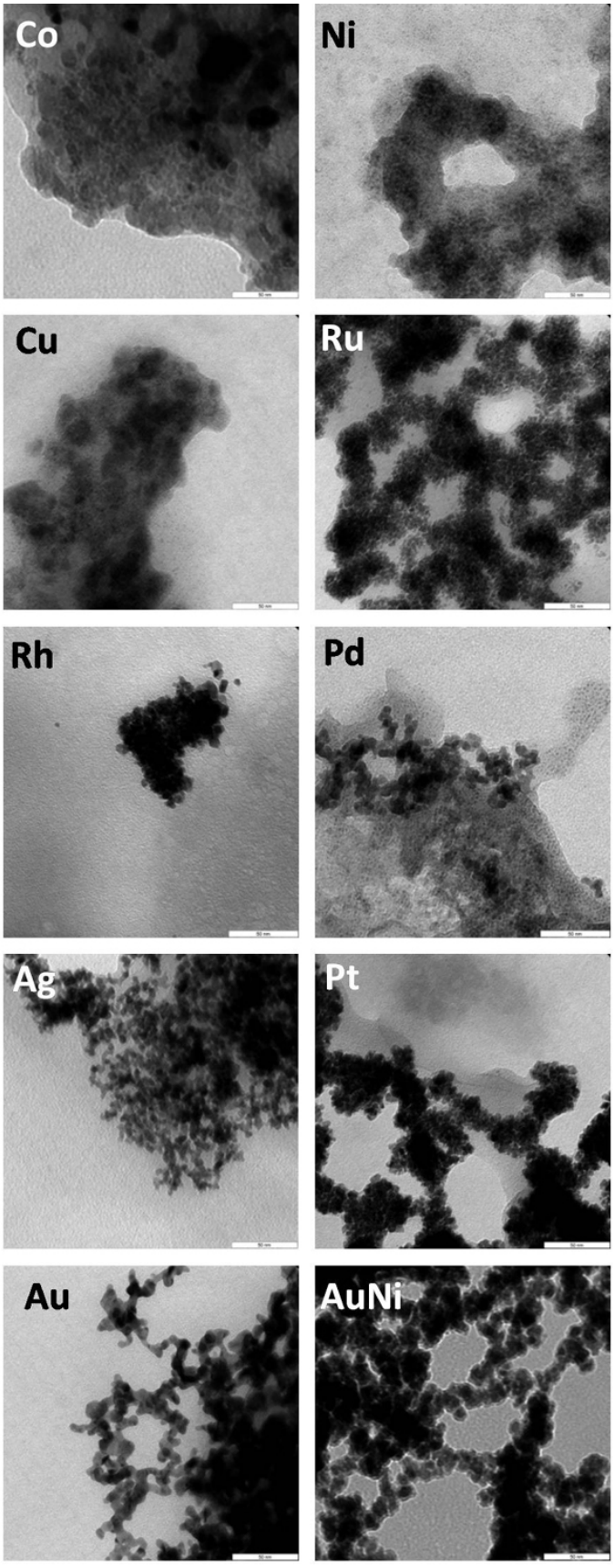

Figure S16. Bright field (BF) TEM images of different metal nanoparticles synthesized without P(triaz) stabilizer, scale bar, 50 nm.

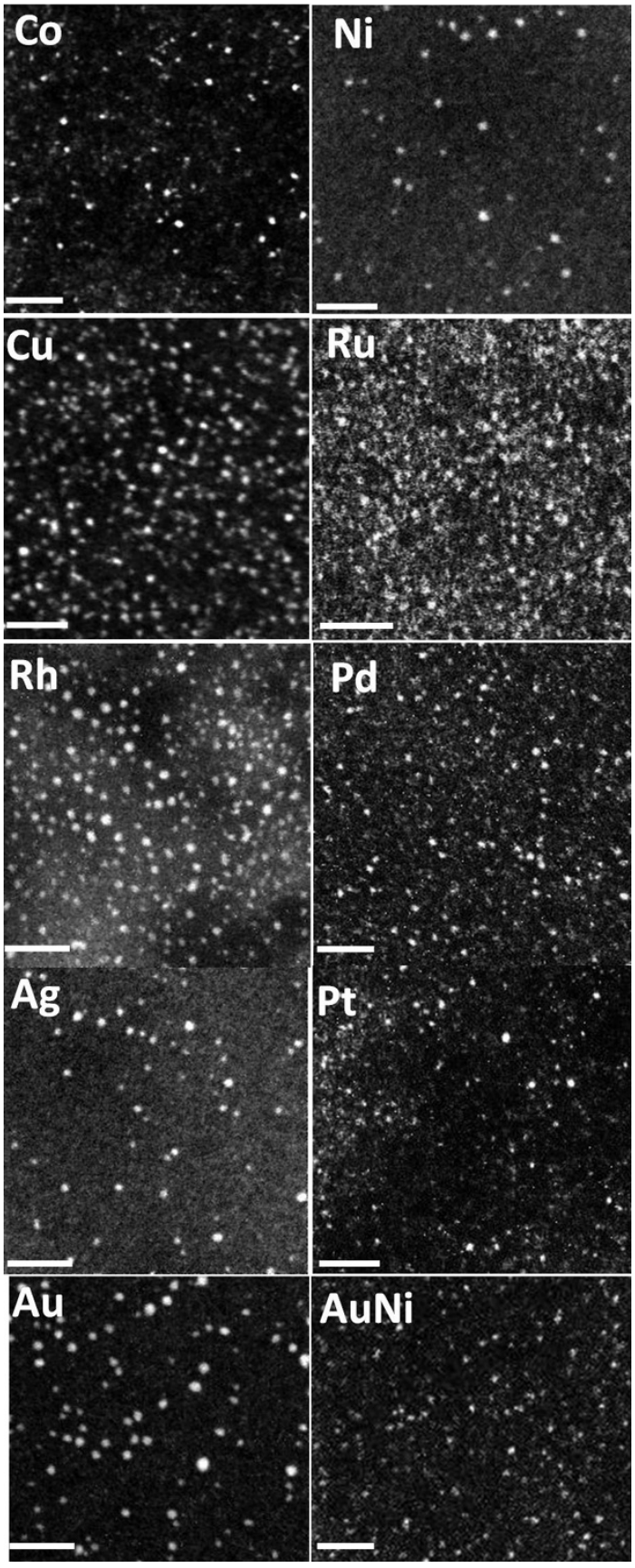

Figure S17. HAADF-STEM images of P(triaz) stabilized MCs with higher magnification, scale bar, 10 nm.

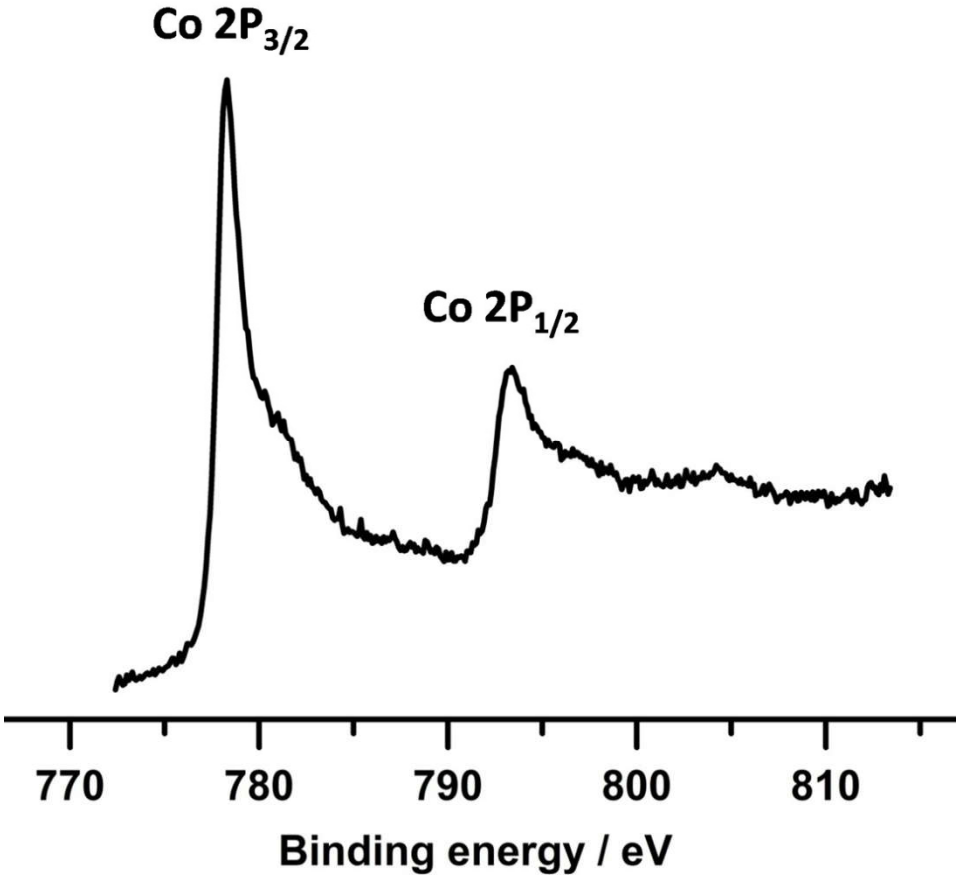

Figure S18. XPS spectrum of Co/P(triaz) showing Co $2p_{3/2}$ (778.3 eV) and $2p_{1/2}$ (793.3 eV) peaks of metallic Co after Ar etching.

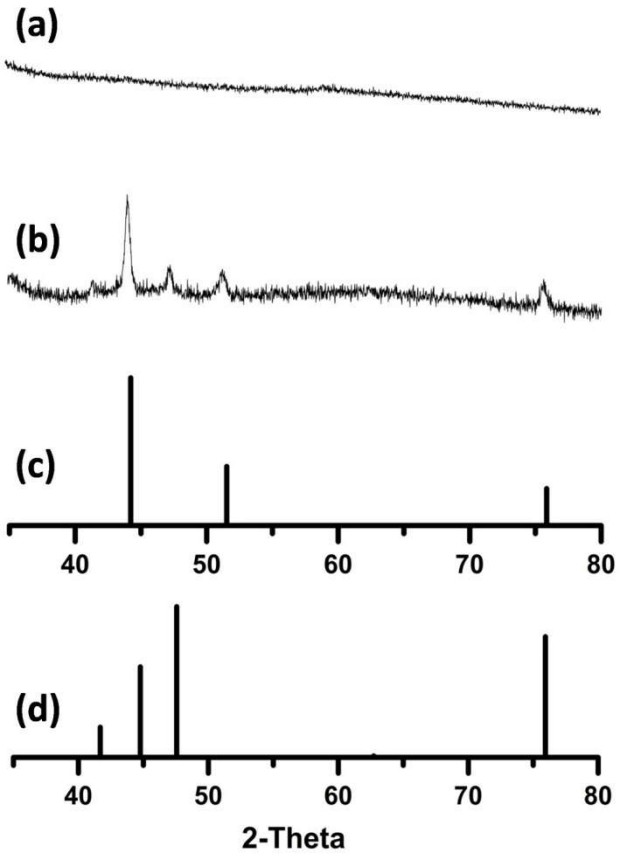

Figure S19. PXRD pattern of (a) the as-synthesized Co/P(triaz) and (b) after annealing at 500 ^{o}C for 3 h in Ar atmosphere. The patterns match well with (c) cubic Co (PDF#15-0806) and (d) hexagonal Co (PDF#05-0727). These experiments demonstrated that metallic Co is formed after reduction by $NaBH_4$.

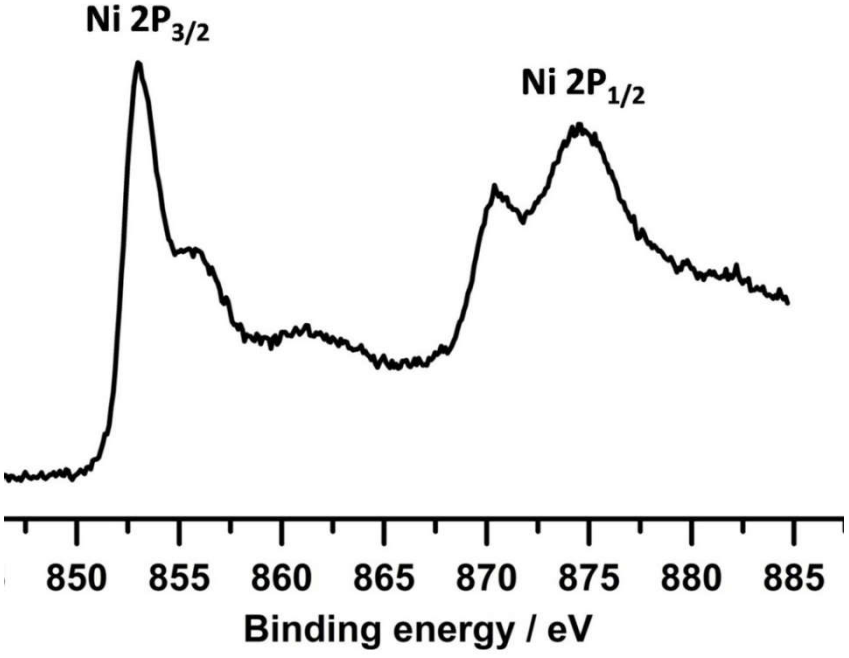

Figure S20. XPS spectrum of Ni/P(triaz) showing Ni $2p_{3/2}$ (852.9 eV) and $2p_{1/2}$ (874.5 eV) peaks of metallic Ni after Ar etching.

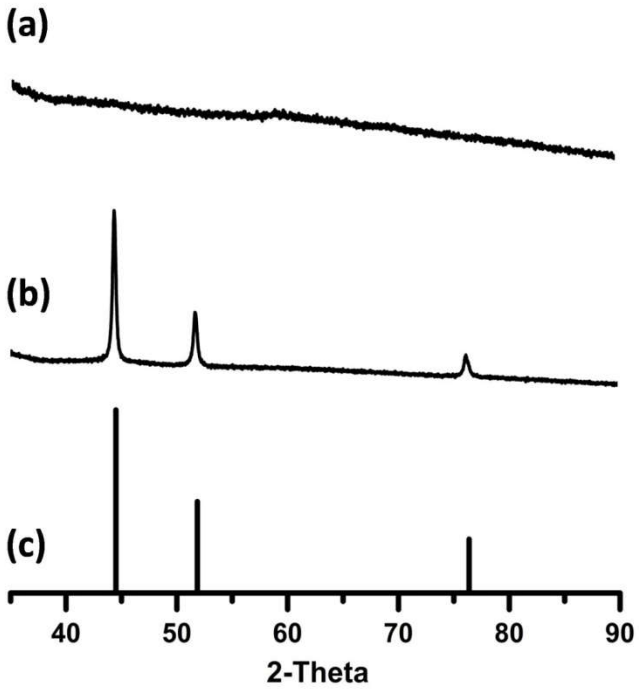

Figure S21. PXRD pattern of (a) the as-synthesized Ni/P(triaz) and (b) after annealing at 500 ^{o}C for 3 h in Ar atmosphere. The patterns match well with (c) cubic Ni (PDF#65-2865). These experiments demonstrated that metallic Ni is formed after reduction by $NaBH_4$.

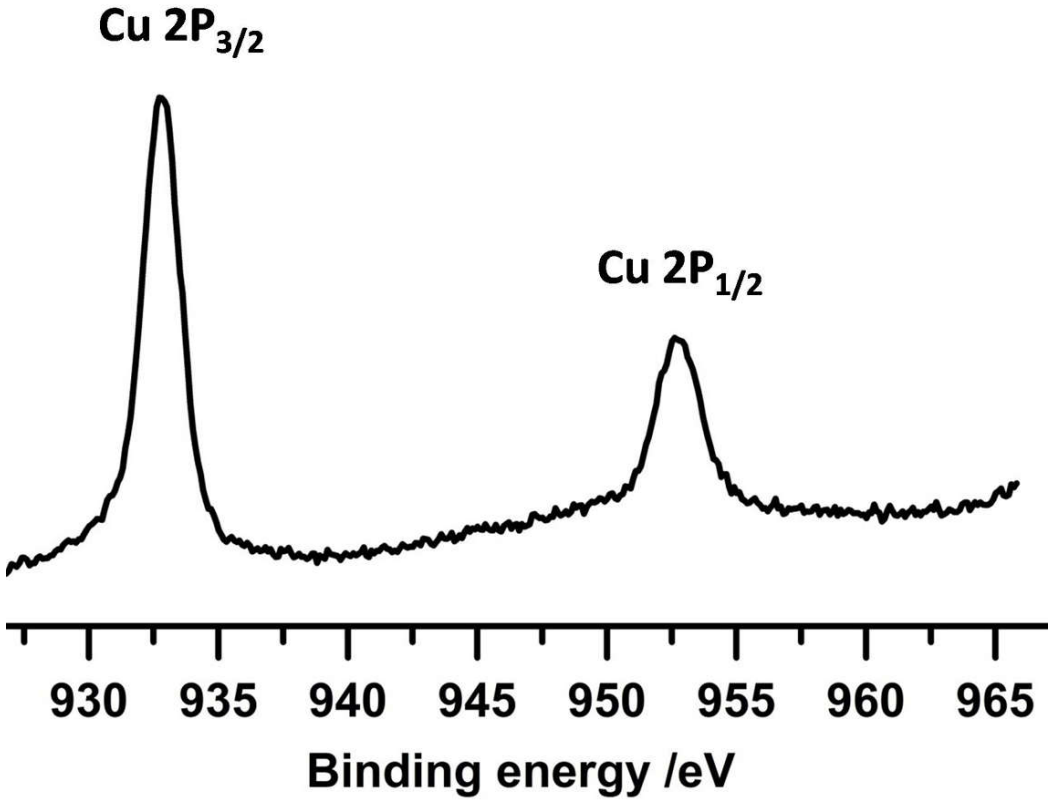

Figure S22. XPS spectrum of Cu/P(triaz) showing Cu $2p_{3/2}$ (932.8 eV) and $2p_{1/2}$ (952.6 eV) peaks of metallic Cu after Ar etching.

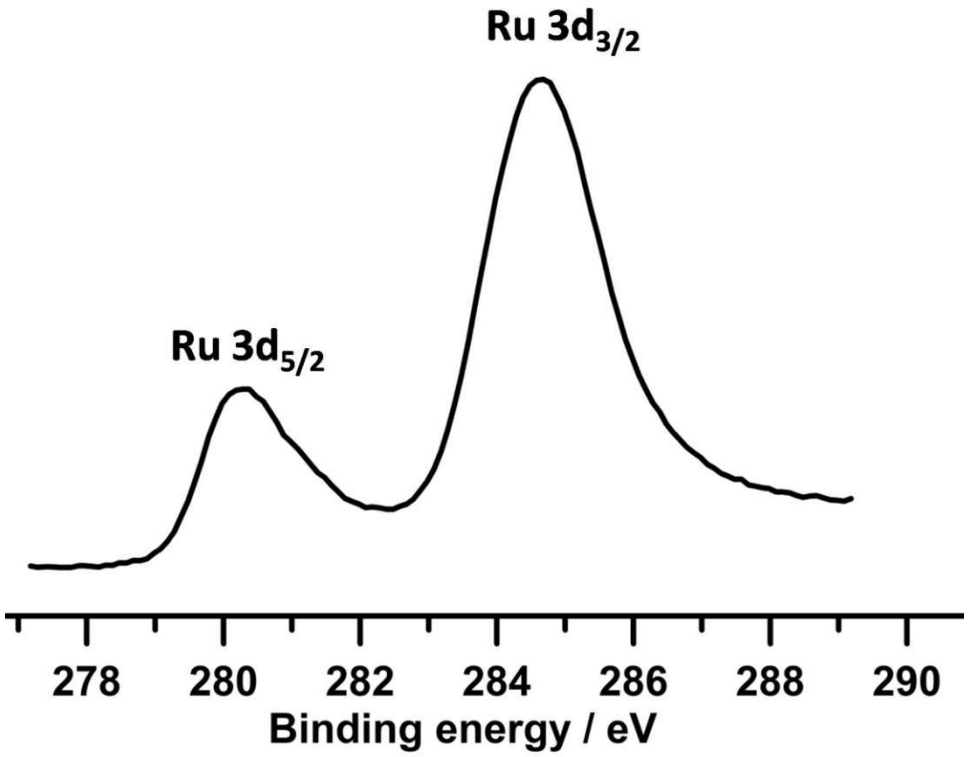

Figure S23. XPS spectrum of Ru/P(triaz) showing Ru $3d_{5/2}$ (280.2 eV) and $3d_{3/2}$ (284.6 eV) peaks of metallic Ru after Ar etching.

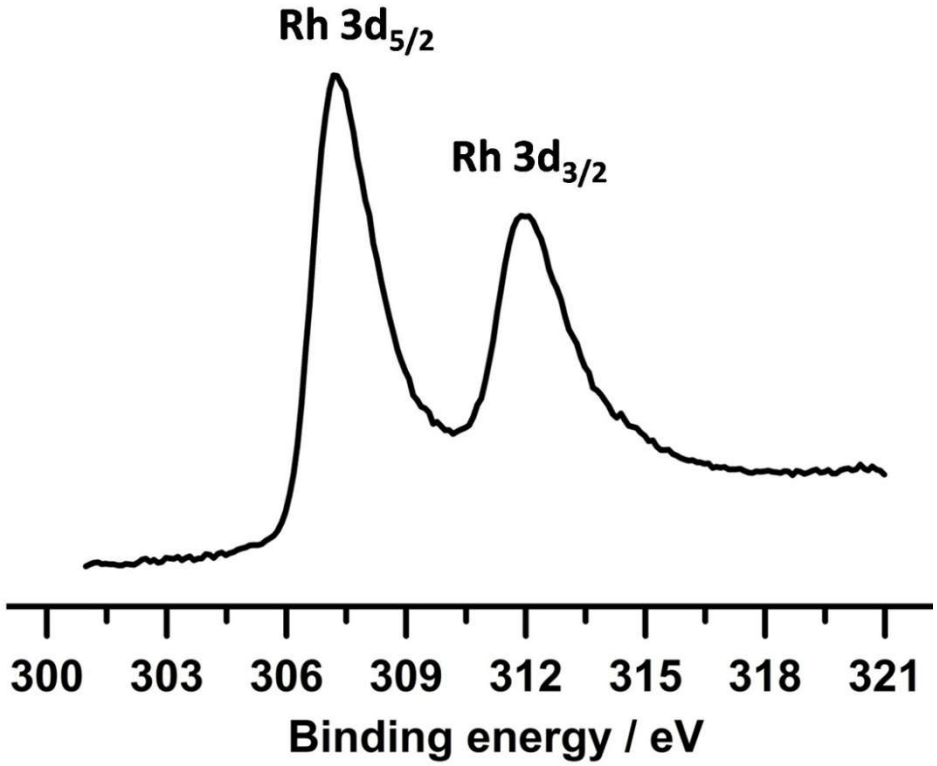

Figure S24. XPS spectrum of Rh/P(triaz) showing Rh $3d_{5/2}$ (307.2 eV) and $3d_{3/2}$ (311.9 eV) peaks of metallic Rh after Ar etching.

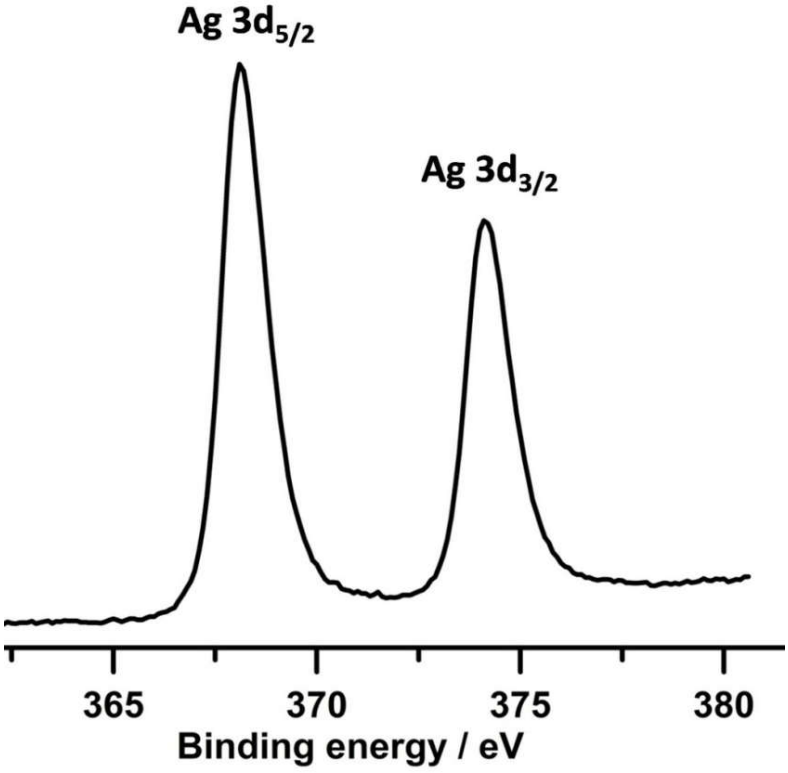

Figure S25. XPS spectrum of Ag/P(triaz) showing Ag $3d_{5/2}$ (368.1 eV) and $3d_{3/2}$ (374.1 eV) peaks of metallic Ag after Ar etching.

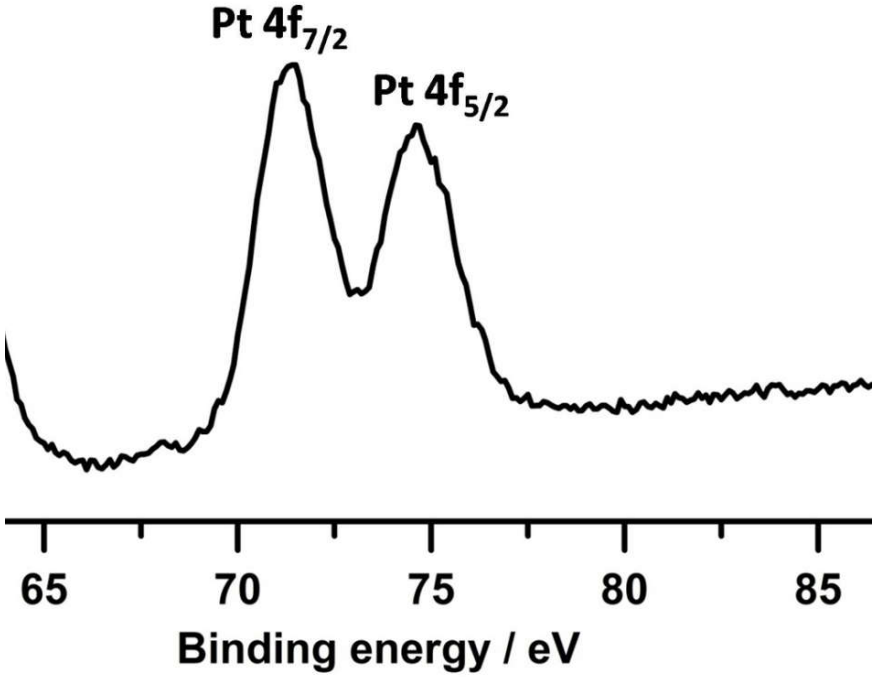

Figure S26. XPS spectrum of Pt/P(triaz) showing Pt $4f_{7/2}$ (71.4 eV) and $4f_{5/2}$ (74.6 eV) peaks of metallic Pt after Ar etching.

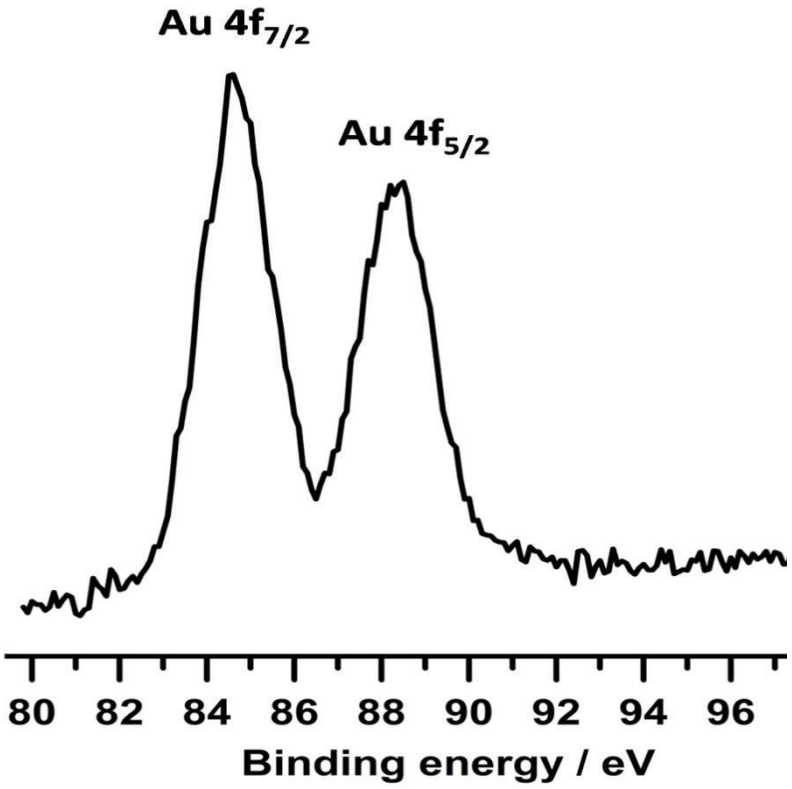

Figure S27. XPS spectrum of Au/P(triaz) showing Au $4f_{7/2}$ (84.4 eV) and $4f_{5/2}$ (88.3 eV) peaks of metallic Au after Ar etching.

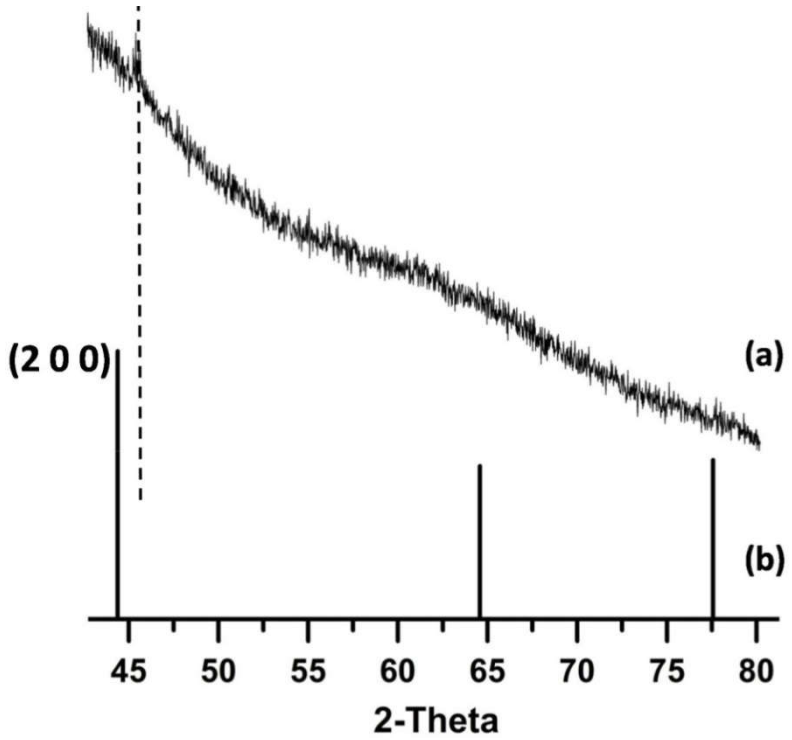

Figure S28. The PXRD patterns of (a) as-synthesized AuNi/P(triaz), (b) positions of reflections for pure Au marked by vertical lines. The (2 0 0) reflections of AuNi/P(triaz) shifted to higher angles (indicated by the dot line) as compared with that of pure Au. This observation indicates that Ni incorporated into the Au *fcc* structure forms an alloy phase.

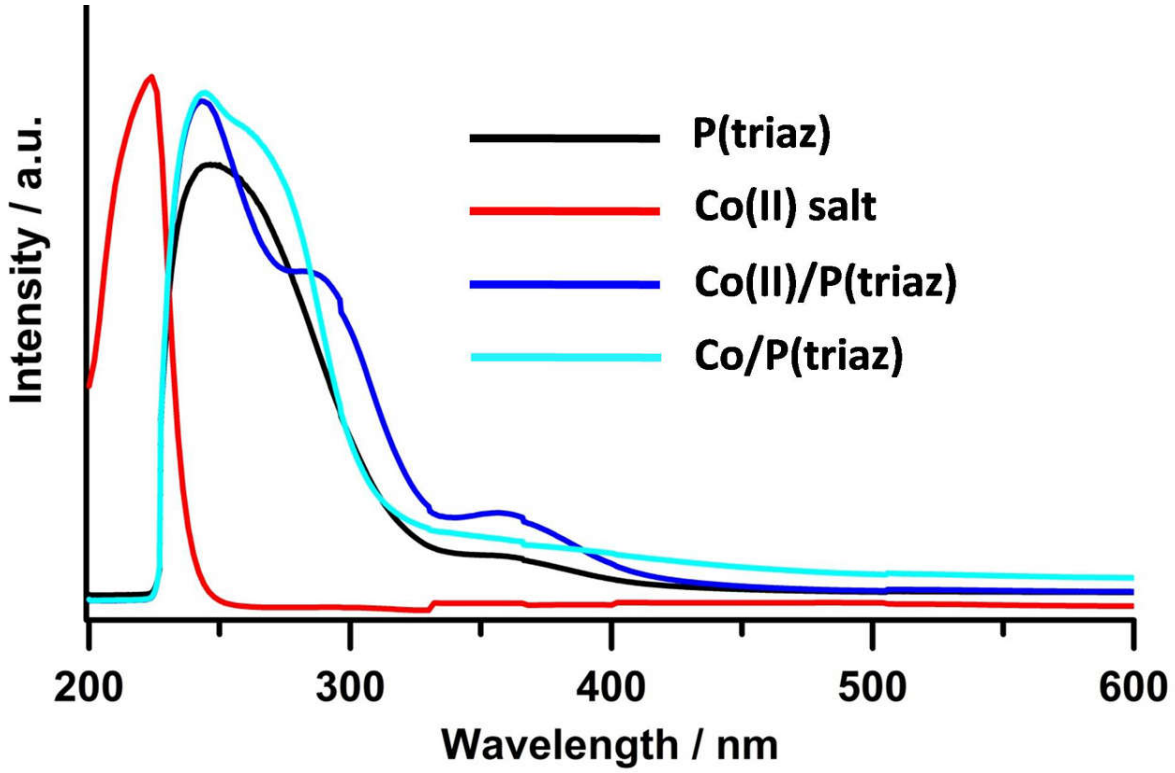

Figure S29. The UV-vis spectra monitoring the formation process of Co/P(triaz) in dichloromethane-methanol mixture (volume ratio = 2:1).

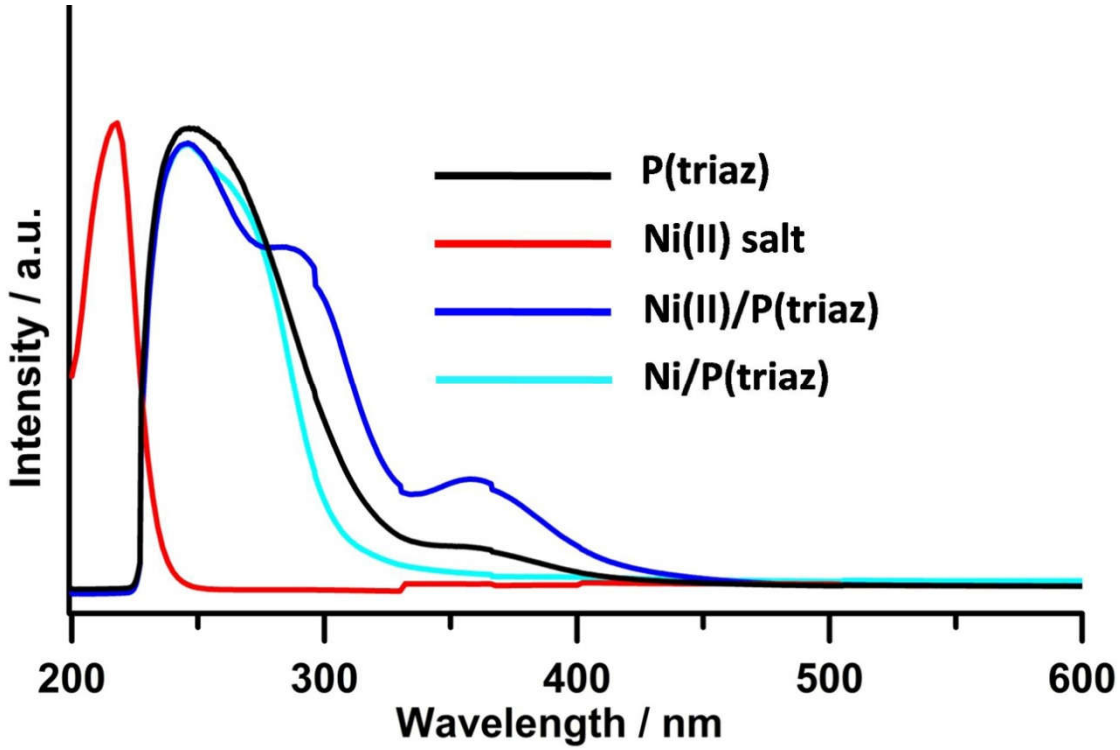

Figure S30. The UV-vis spectra monitoring the formation process of Ni/P(triaz) in dichloromethane-methanol mixture (volume ratio = 2:1).

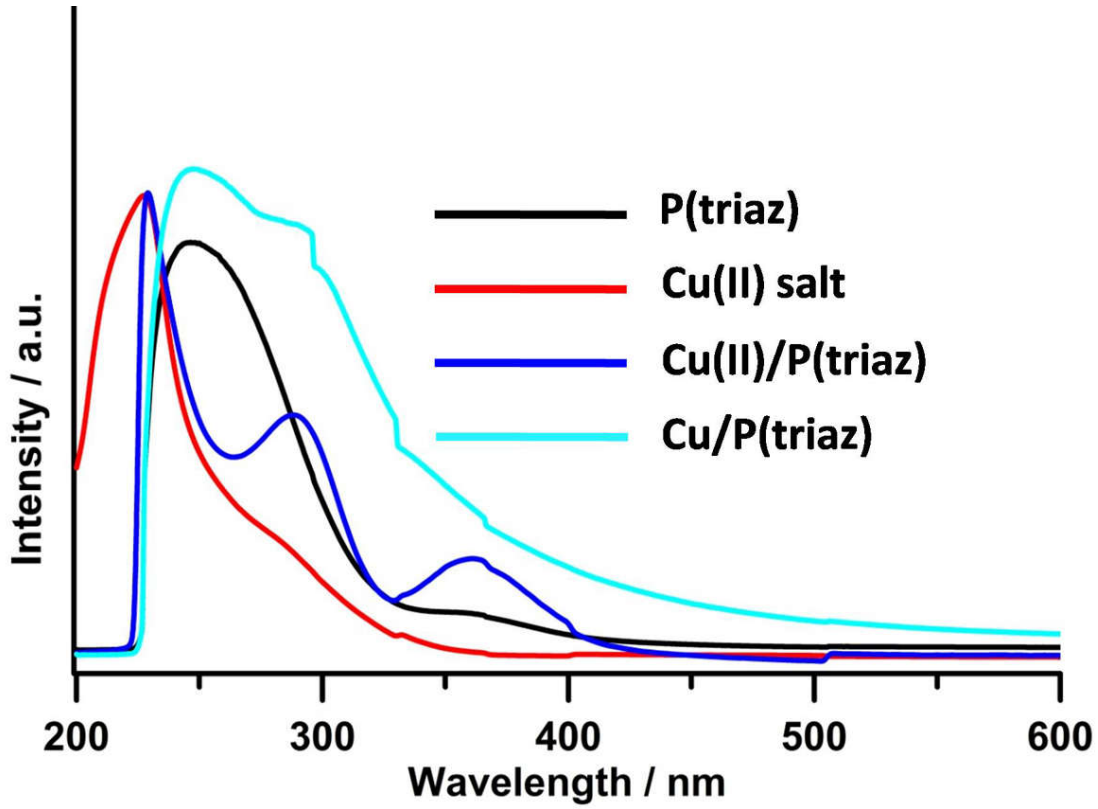

Figure S31. The UV-vis spectra monitoring the formation process of Cu/P(triaz) in dichloromethane-methanol mixture (volume ratio = 2:1).

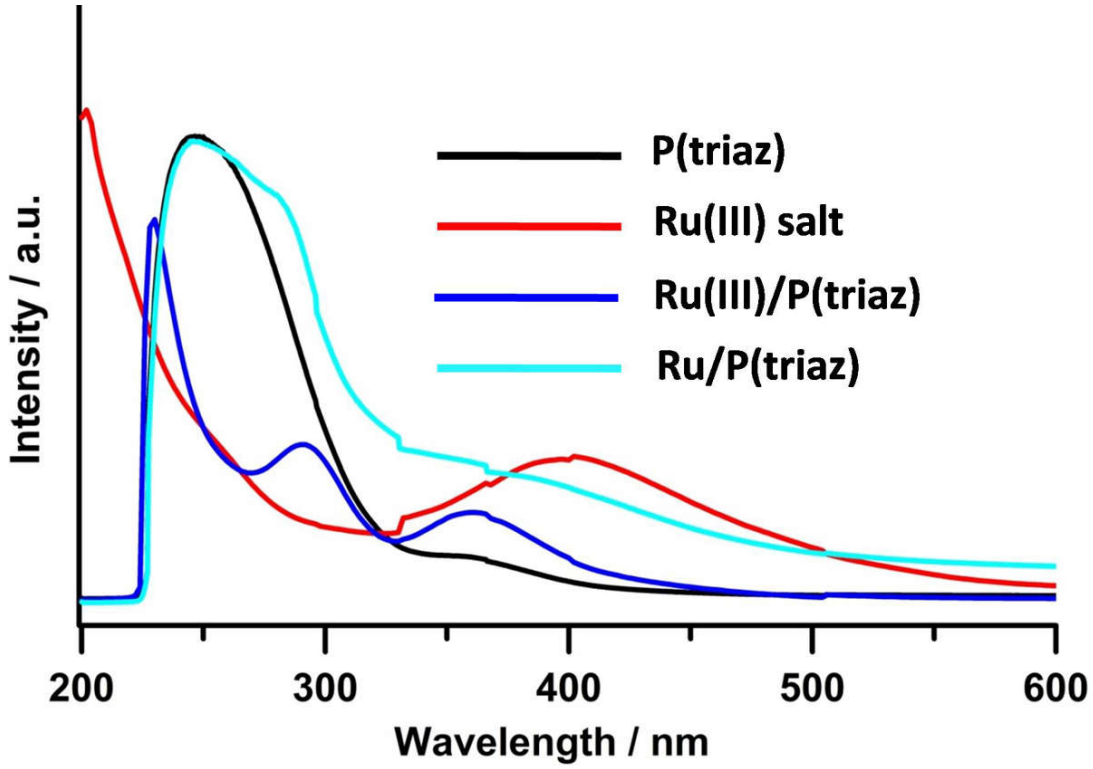

Figure S32. The UV-vis spectra monitoring the formation process of Ru/P(triaz) in dichloromethane-methanol mixture (volume ratio = 2:1).

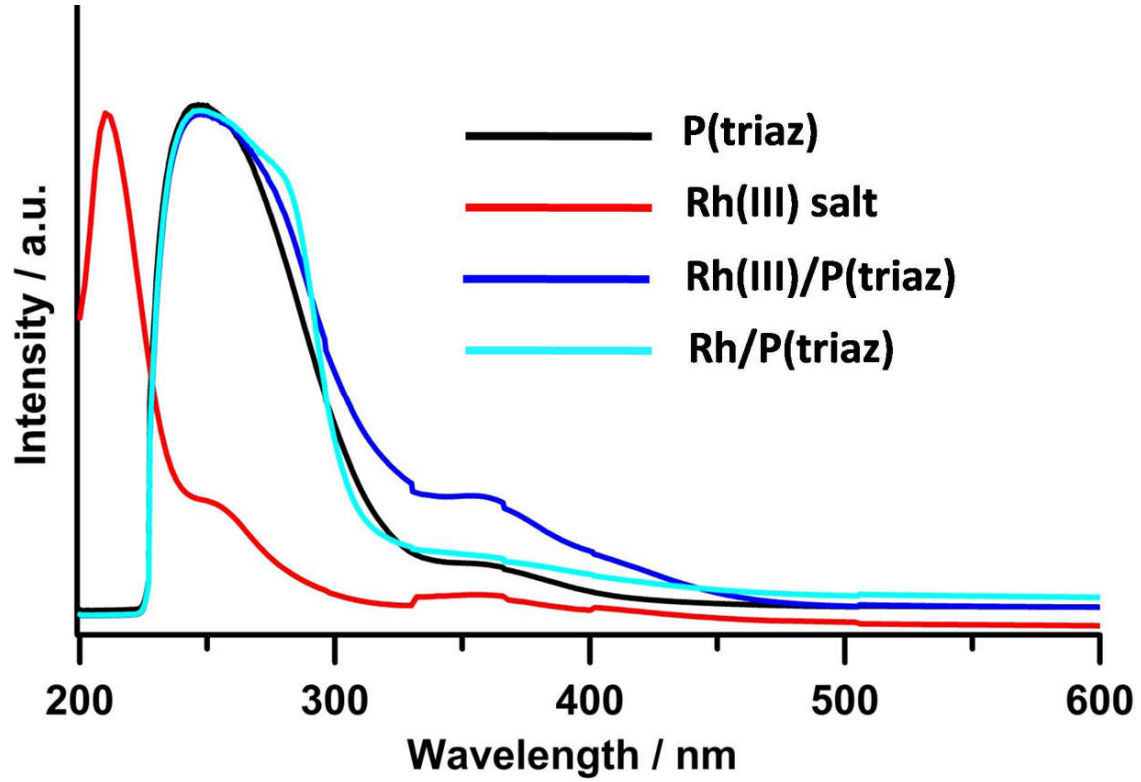

Figure S33. The UV-vis spectra monitoring the formation process of Rh/P(triaz) in dichloromethane-methanol mixture (volume ratio = 2:1).

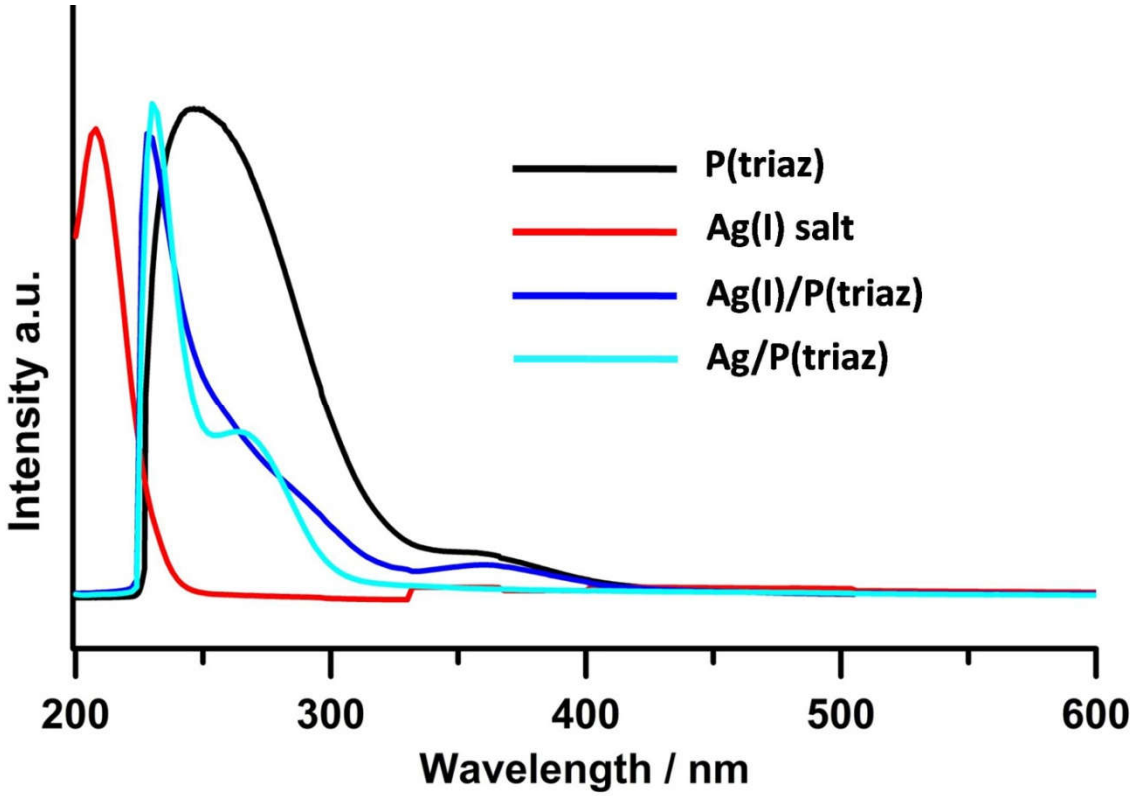

Figure S34. The UV-vis spectra monitoring the formation process of Ag/P(triaz) in dichloromethane-methanol mixture (volume ratio = 2:1).

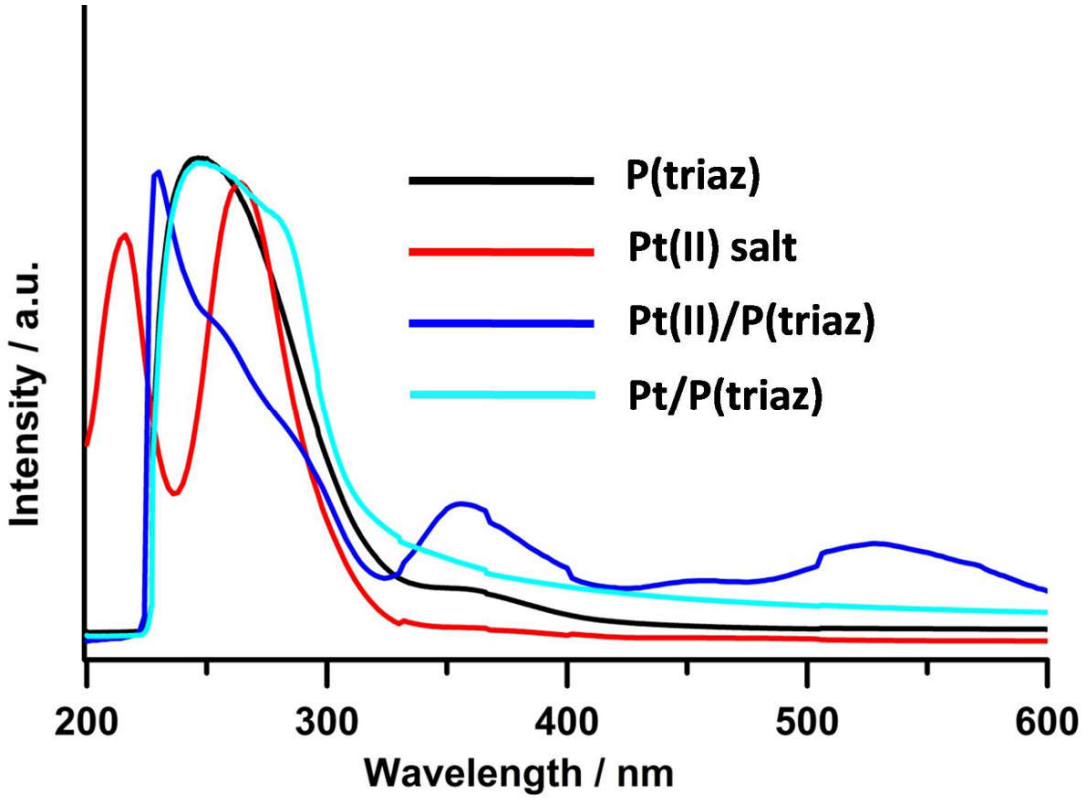

Figure S35. The UV-vis spectra monitoring the formation process of Pt/P(triaz) in dichloromethane-methanol mixture (volume ratio = 2:1).

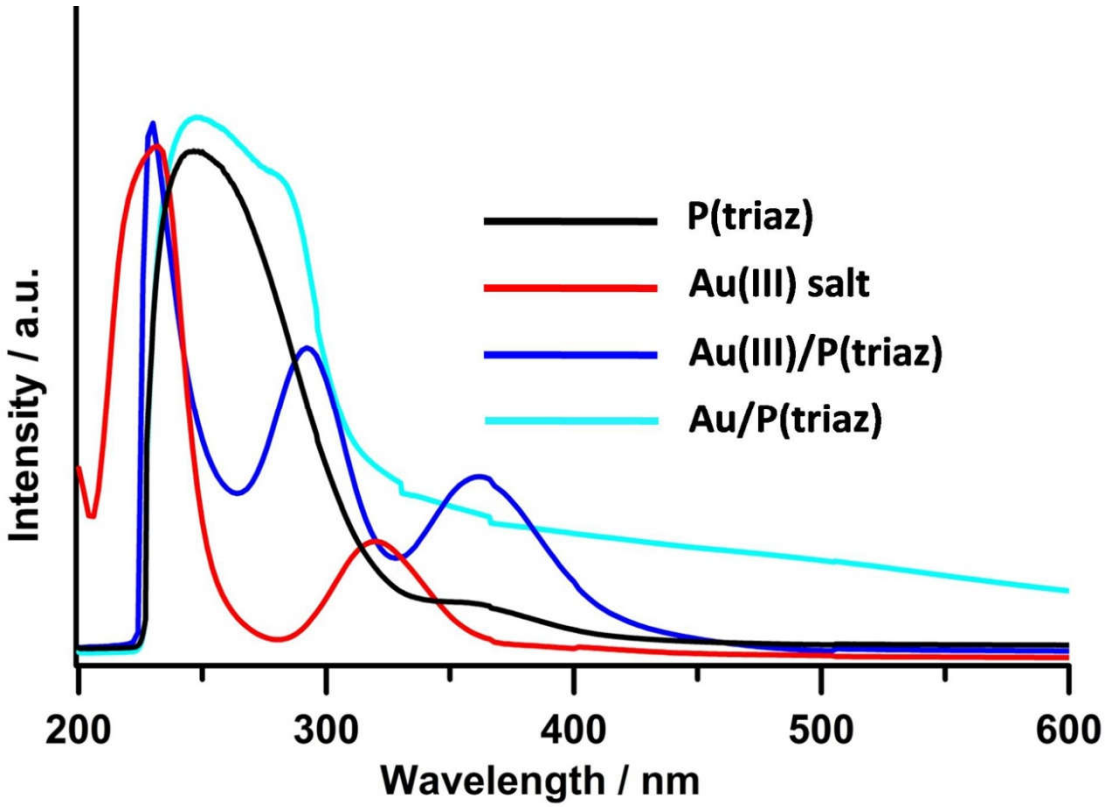

Figure S36. The UV-vis spectra monitoring the formation process of Au/P(triaz) in dichloromethane-methanol mixture (volume ratio = 2:1).

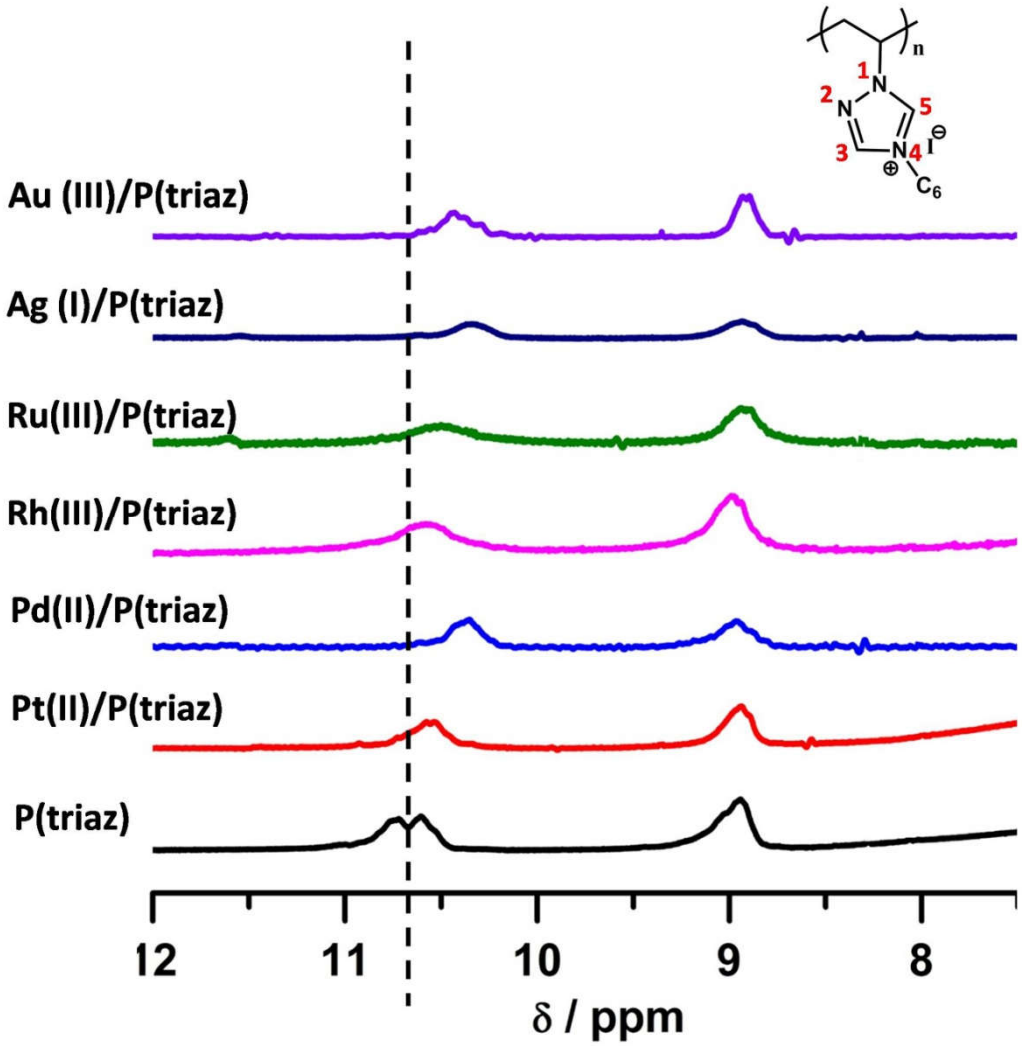

Figure S37. ^{1}H NMR spectra of native P(triaz) and P(triaz) after mixing with different metal ion species (denoted as metal ion/P(triaz)) in CD_2Cl_2 and CH_3OH (volume ratio = 2:1). An obvious shift of the H atom at C5 position (C-5 proton) to high magnetic field could be observed (shown in dot line) in metal ion/P(triaz) as compared with that of pure P(triaz), which is indicative of the coordination between the metal ions and P(triaz).

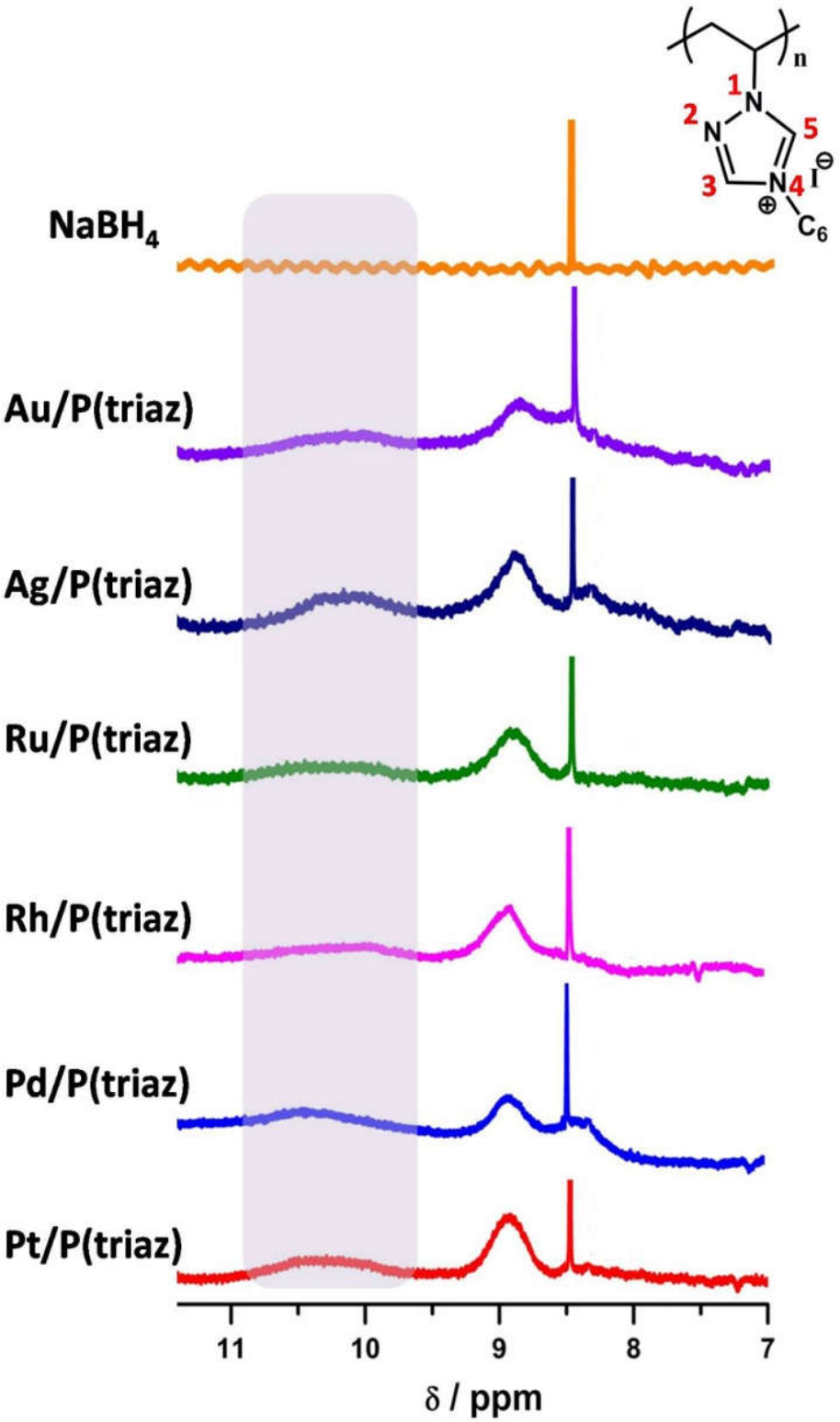

Figure S38. ^{1}H NMR spectra of metal ion/P(triaz) after adding $NaBH_4$ (denoted as MC/P(triaz)) in CD_2Cl_2 and CH_3OH mixture (volume ratio = 2:1). The signal at 8.5 ppm in all spectra is attributed to the influence of the $NaBH_4$ as demonstrated by a control experiment via direct adding $NaBH_4$ into a CD_2Cl_2 and CH_3OH mixture (the yellow line in the top). The C-5 proton (10.6 ppm) in MC/P(triaz) decreased its intensity, indicating that P(triaz) *in situ* generates the polycarbene during the MC formation process.

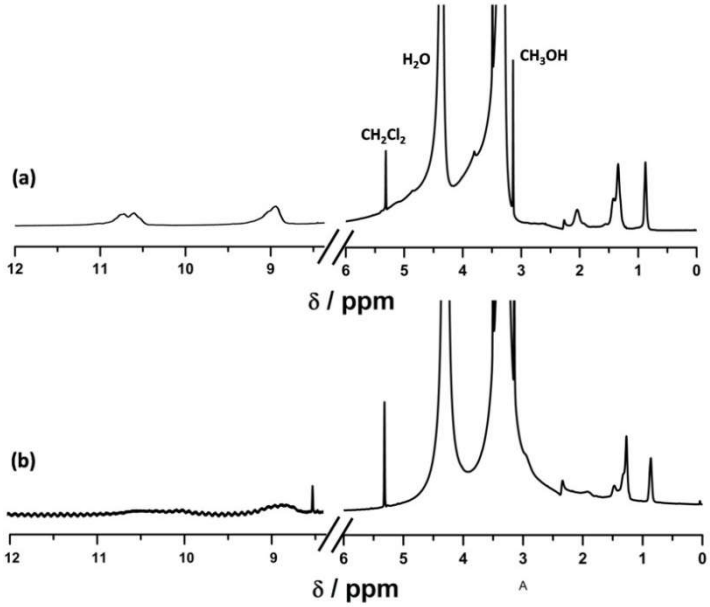

Figure S39. ^{1}H-NMR spectra of P(triaz) in CD_2Cl_2 and CH_3OH mixture (volume ratio = 2:1) before (a) and after (b) adding $NaBH_4$. The signal at 8.5 ppm in spectra (b) is attributed to $NaBH_4$ in the mixture CD_2Cl_2 and CH_3OH (volume ratio = 2:1). The characteristic peaks maintain after adding $NaBH_4$ except the decreased intensity of C-5 protons. This indicates that the chemical structure of P(triaz) is stable in the MC formation process.

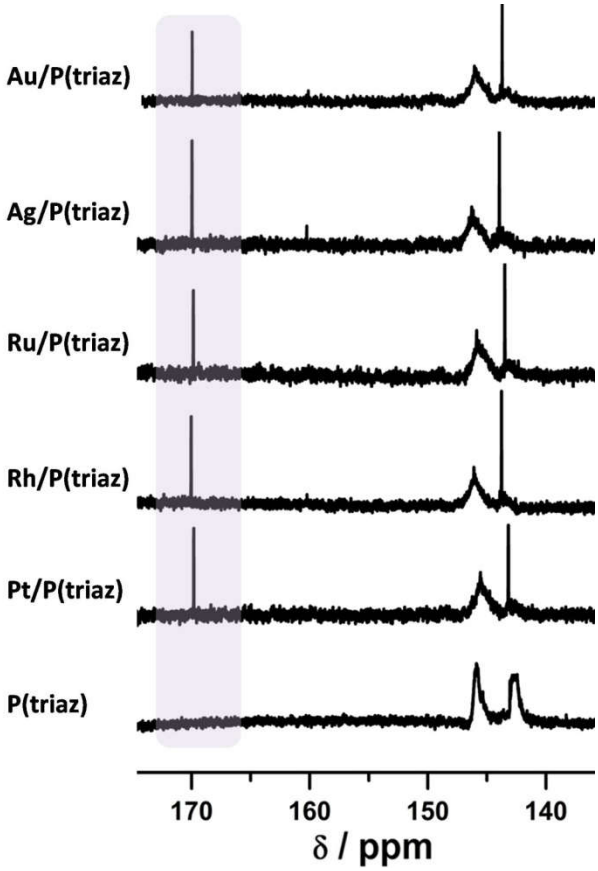

Figure S40. ^{13}C NMR spectra of P(triaz), MCs/P(triaz) in CD_2Cl_2 and CH_3OH mixture (volume ratio = 2:1). The strong intensive peaks at around 170 ppm appeared in MCs/P(triaz) (shown in violet rectangle), typical chemical shifts for metal-carbene coordination.

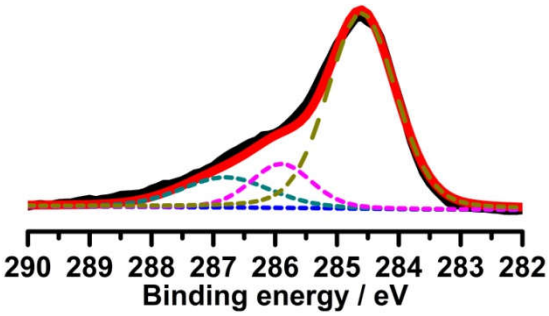

Figure S41. XPS spectra for C 1s signals of Co/P(triaz). The C1s spectra could be fitted by the sum of three separated peaks (dotted lines) with 1:1:8 area ratios that correspond to C5 (286.8 eV), C3 (285.9 eV) and eight alkane carbons (284.6 eV) in PIL. The C5 component shifts 0.4 eV to lower binding energy in Co/P(triaz) as compared with that of P(triaz) due to the Co-carbene complexation.

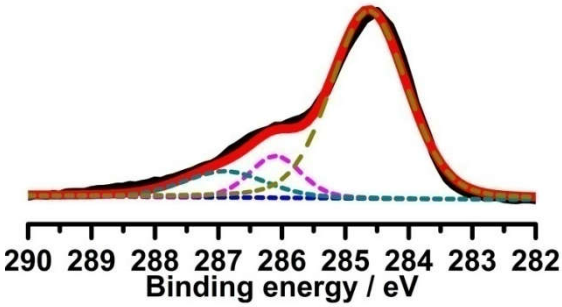

Figure S42. XPS spectra for C 1s signals of Ni/P(triaz). The C1s spectra could be fitted by the sum of three separated peaks (dotted lines) with 1:1:8 area ratios that correspond to C5 (286.9 eV), C3 (286.1 eV) and eight alkane carbons (284.6 eV) in PIL. The C5 component shifts 0.3 eV to lower binding energy in Ni/P(triaz) as compared with that of P(triaz) due to the Ni-carbene complexation.

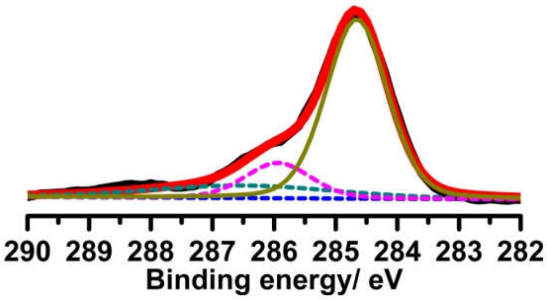

Figure S43. XPS spectra for C 1s signals of Cu/P(triaz). The C1s spectra could be fitted by the sum of three separated peaks (dotted lines) with 1:1:8 area ratios that correspond to C5 (286.7 eV), C3 (286.0 eV) and eight alkane carbons (284.6 eV) in PIL. The C5 component shifts 0.5 eV to lower binding energy in Cu/P(triaz) as compared with that of P(triaz) due to the Cu-carbene complexation.

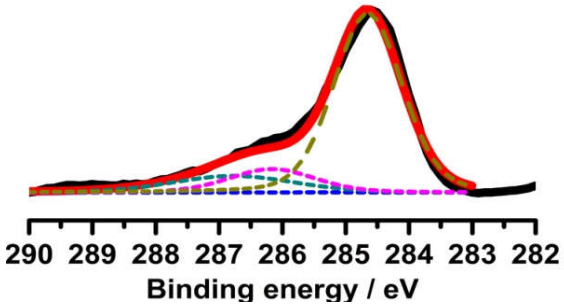

Figure S44. XPS spectra for C 1s signals of Ru/P(triaz). The C1s spectra could be fitted by the sum of three separated peaks (dotted lines) with 1:1:8 area ratios that correspond to C5 (286.8 eV), C3 (286.1 eV) and eight alkane carbons (284.6 eV) in PIL. The C5 component shifts 0.4 eV to lower binding energy in Ru/P(triaz) as compared with that of P(triaz) due to the Ru-carbene complexation.

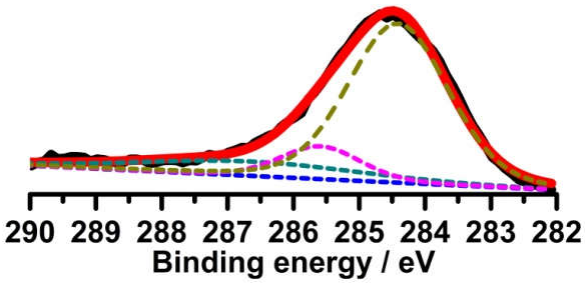

Figure S45. XPS spectra for C 1s signals of Rh/P(triaz). The C1s spectra could be fitted by the sum of three separated peaks (dotted lines) with 1:1:8 area ratios that correspond to C5 (286.6 eV), C3 (286.1 eV) and eight alkane carbons (284.6 eV) in PIL. The C5 component shifts 0.6 eV to lower binding energy in Rh/P(triaz) as compared with that of P(triaz) due to the Rh-carbene complexation.

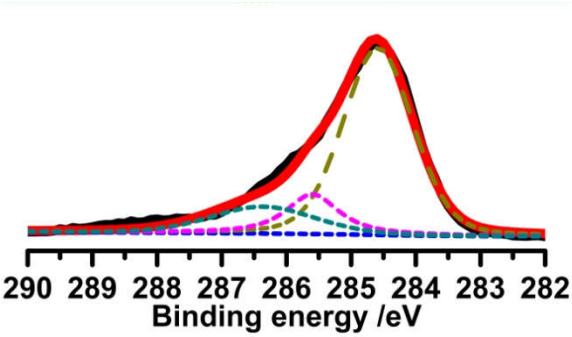

Figure S46. XPS spectra for C 1s signals of Ag/P(triaz). The C1s spectra could be fitted by the sum of three separated peaks (dotted lines) with 1:1:8 area ratios that correspond to C5 (286.4 eV), C3 (285.6 eV) and eight alkane carbons (284.6 eV) in PIL. The C5 component shifts 0.8 eV to lower binding energy in Ag/P(triaz) as compared with that of P(triaz) due to the Ag-carbene complexation.

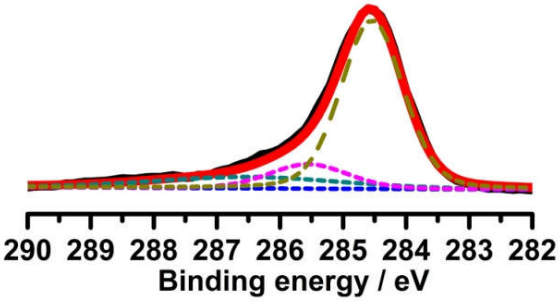

Figure S47. XPS spectra for C 1s signals of Pt/P(triaz). The C1s spectra could be fitted by the sum of three separated peaks (dotted lines) with 1:1:8 area ratios that correspond to C5 (286.8 eV), C3 (285.6 eV) and eight alkane carbons (284.6 eV) in PIL. The C5 component shifts 0.4 eV to lower binding energy in Pt/P(triaz) as compared with that of P(triaz) due to the Pt-carbene complexation.

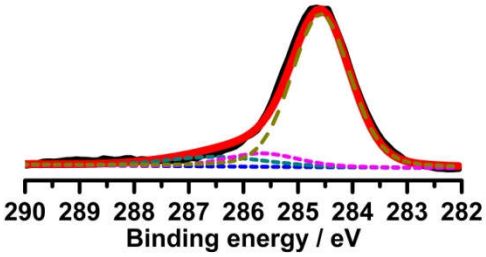

Figure S48. XPS spectra for C 1s signals of Au/P(triaz). The C1s spectra could be fitted by the sum of three separated peaks (dotted lines) with 1:1:8 area ratios that correspond to C5 (286.4 eV), C3 (285.6 eV) and eight alkane carbons (284.6 eV) in PIL. The C5 component shifts 0.8 eV to lower binding energy in Au/P(triaz) as compared with that of P(triaz) due to the Au-carbene complexation.

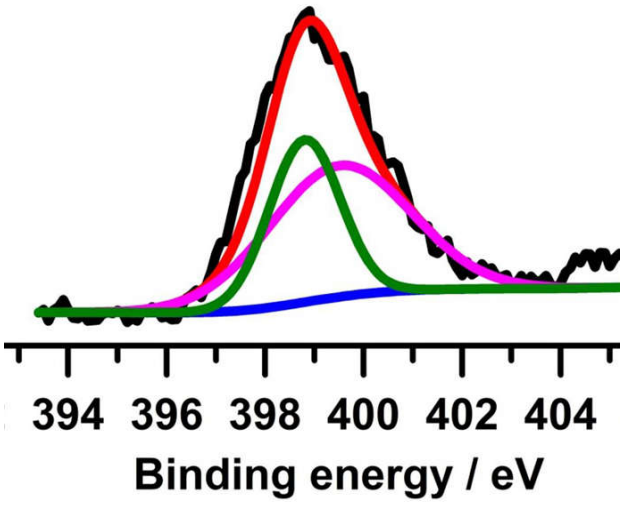

Figure S49. XPS spectra for N 1s signals of Co/P(triaz). N1s spectra could be fitted by the sum of two separate peaks (at 398.8 and 399.6 eV) with a ratio of 1:2 in their integration that correspond to naked nitrogen (N2) and the two other nitrogen atoms (N1 and N4) of the

triazolium ring, respectively. Compared with the P(triaz) (N2 at 398.6 eV) (Figure 3d in main text), a shift of binding energy of N2 toward high position could be observed in Co/P(triaz), which could be attributed to the resultant binding to the metal.

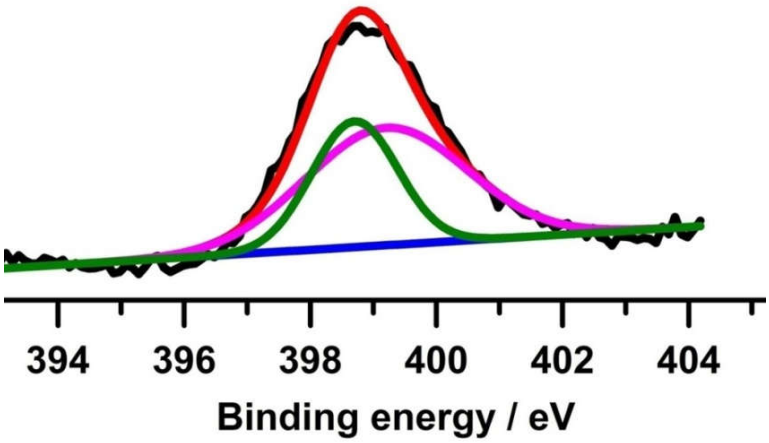

Figure S50. XPS spectra for N 1s signals of Ni/P(triaz). XPS spectra for N 1s signals of Ni/P(triaz). N1s spectra could be fitted by the sum of two separate peaks (at 398.8 and 399.2 eV) with a ratio of 1:2 in their integration area that correspond to naked nitrogen (N2) and the two other nitrogen atoms (N1 and N4) of the triazolium ring, respectively. Compared with the P(triaz) (N2 at 398.6 eV), a shift of binding energy of N2 toward high position could be observed in Ni/P(triaz), which could be attributed to the resultant binding to the metal.

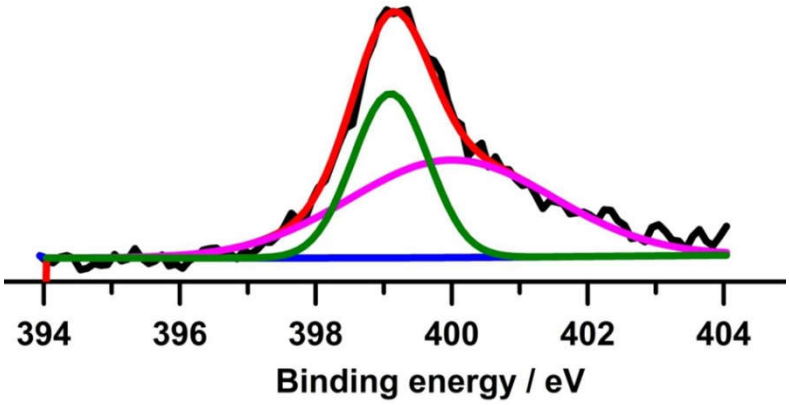

Figure S51. XPS spectra for N 1s signals of Cu/P(triaz). N1s spectra could be fitted by the sum of two separate peaks (at 399.1 and 400 eV) with a ratio of 1:2 in their integration area that correspond to naked nitrogen (N2) and the two other nitrogen atoms (N1 and N4) of the triazolium ring, respectively. Compared with the P(triaz) (N2 at 398.6 eV), a shift of binding energy of N2 toward high position could be observed in Cu/P(triaz), which could be attributed to the resultant binding to the metal.

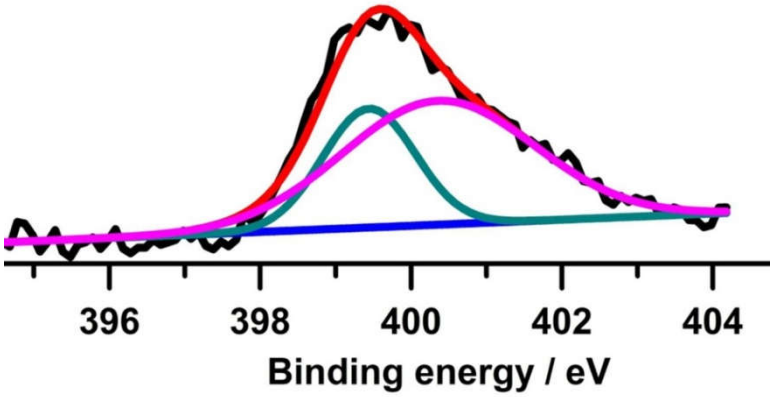

Figure S52. XPS spectra for N 1s signals of Ru/P(triaz). N1s spectra could be fitted by the sum of two separate peaks (at 399.5 and 400.4 eV) with a ratio of 1:2 in their integration area that correspond to naked nitrogen (N2) and the two other nitrogen atoms (N1 and N4) of the triazolium ring, respectively. Compared with the P(triaz) (N2 at 398.6 eV), a shift of binding energy of N2 toward high position could be observed in Ru/P(triaz), which could be attributed to the resultant binding to the metal.

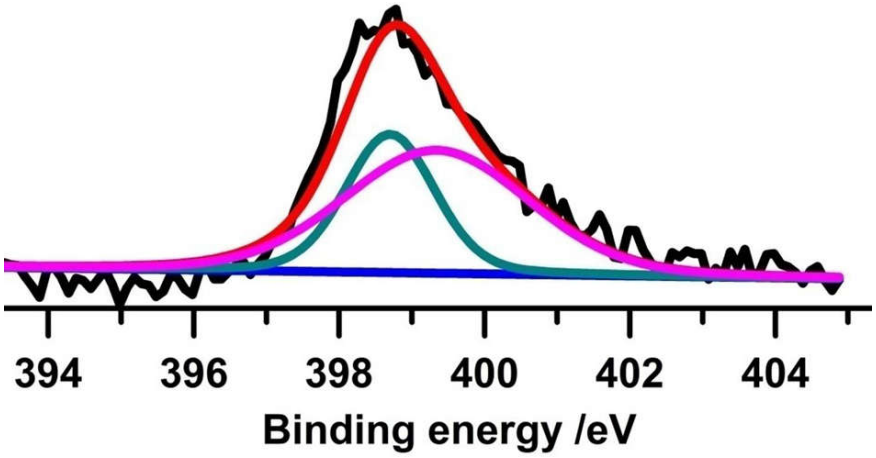

Figure S53. XPS spectra for N 1s signals of Rh/P(triaz). N1s spectra could be fitted by the sum of two separate peaks (at 398.7 and 399.4 eV) with a ratio of 1:2 in their integration area that correspond to naked nitrogen (N2) and the two other nitrogen atoms (N1 and N4) of the triazolium ring, respectively. Compared with the P(triaz) (N2 at 398.6 eV), a shift of binding energy of N2 toward high position could be observed in Rh/P(triaz), which could be attributed to the resultant binding to the metal.

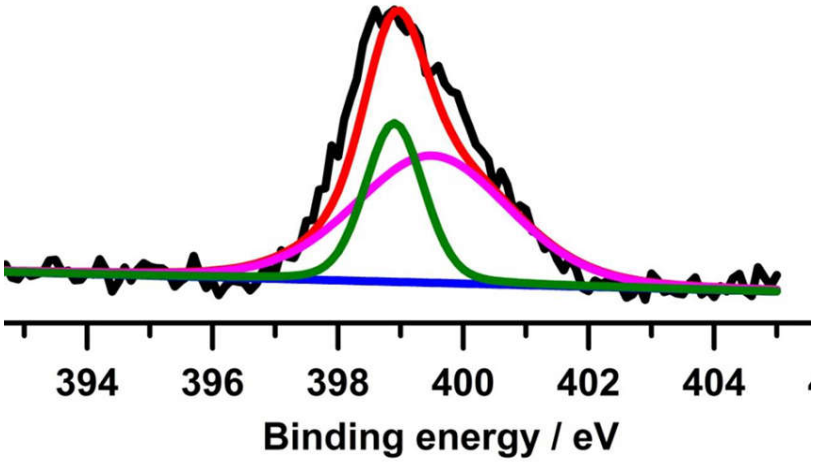

Figure S54. XPS spectra for N 1s signals of Ag/P(triaz). N1s spectra could be fitted by the sum of two separate peaks (at 398.9 and 399.5 eV) with a ratio of 1:2 in their integration area that correspond to naked nitrogen (N2) and the two other nitrogen atoms (N1 and N4) of the triazolium ring, respectively. Compared with the P(triaz) (N2 at 398.6 eV), a shift of binding energy of N2 toward high position could be observed in Ag/P(triaz), which could be attributed to the resultant binding to the metal.

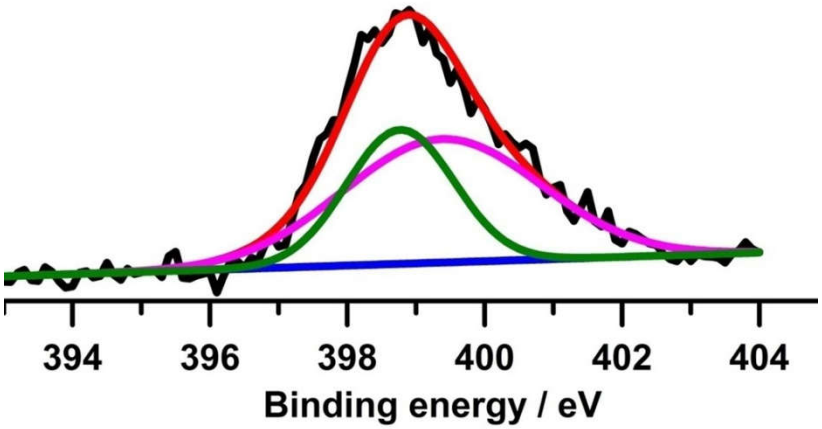

Figure S55. XPS spectra for N 1s signals of Pt/P(triaz). N1s spectra could be fitted by the sum of two separate peaks (at 398.8 and 399.4 eV) with a ratio of 1:2 in their integration area that correspond to naked nitrogen (N2) and the two other nitrogen atoms (N1 and N4) of the triazolium ring, respectively. Compared with the P(triaz) (N2 at 398.6 eV), a shift of binding energy of N2 toward high position could be observed in Pt/P(triaz), which could be attributed to the resultant binding to the metal.

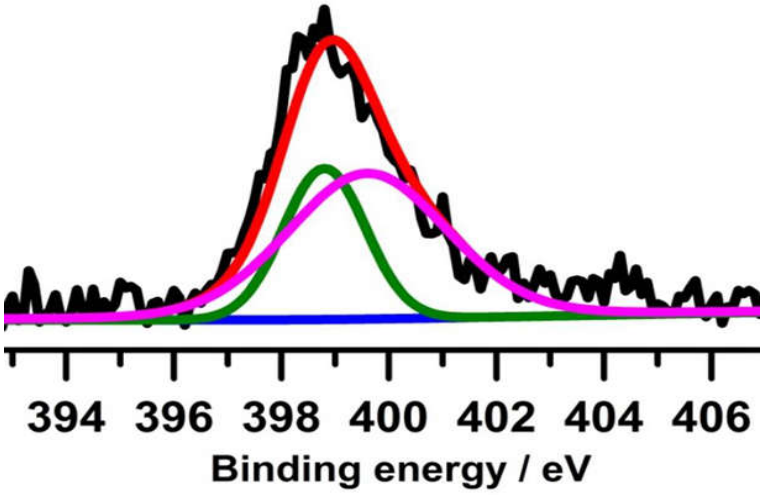

Figure S56. XPS spectra for N 1s signals of Au/P(triaz). N1s spectra could be fitted by the sum of two separate peaks (at 398.8 and 399.6 eV) with a ratio of 1:2 in their integration area that correspond to naked nitrogen (N2) and the two other nitrogen atoms (N1 and N4) of the triazolium ring, respectively. Compared with the P(triaz) (N2 at 398.6 eV), a shift of binding energy of N2 toward high position could be observed in Au/P(triaz), which could be attributed to the resultant binding to the metal.

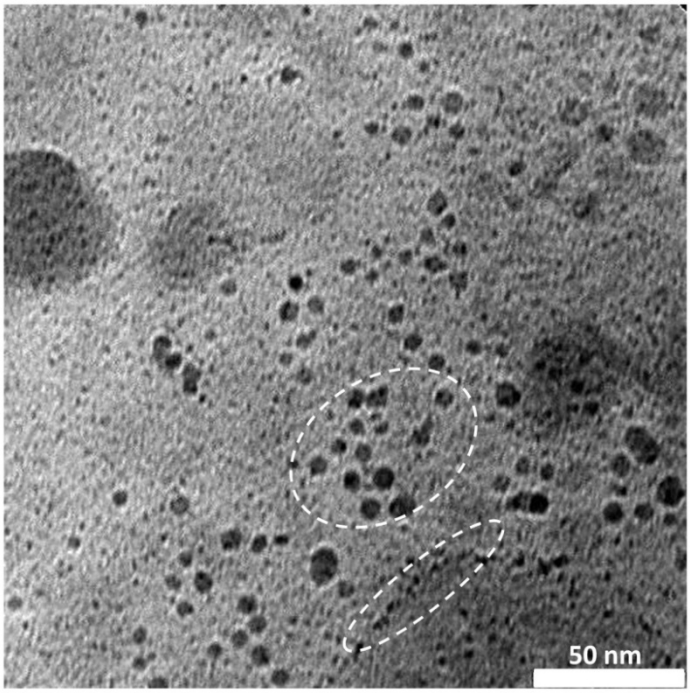

Figure S57. The bright field (BF) TEM image of Pd/PIL-imidaz. The white circles indicate that both clusters and large nanoparticles exist.

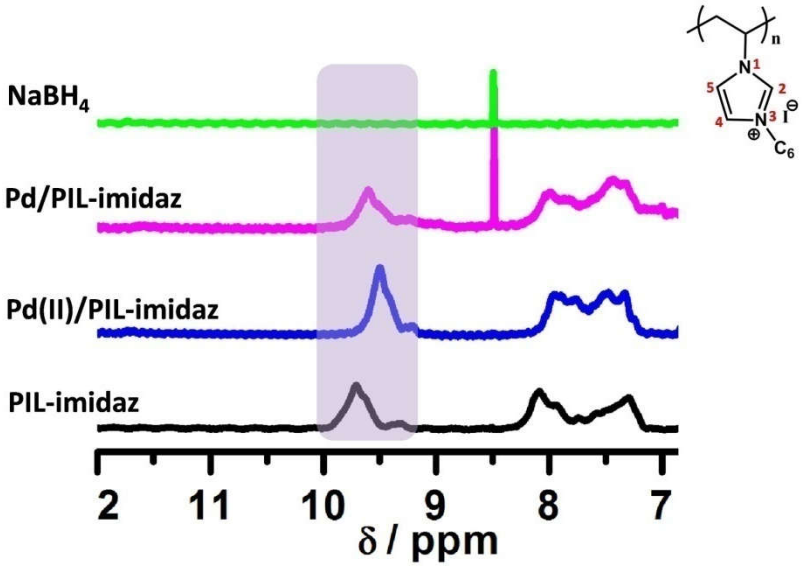

Figure S58. The ^{1}H NMR spectra recorded the formation process of Pd/PIL-imidaz in a CD_2Cl_2 and CH_3OH mixture (volume ratio = 2:1). The signal of H atom at C2 position (9.7 ppm) in native PIL-imidaz remains in Pd/PIL-imidaz after addition of $NaBH_4$ (shown in violet rectangle), indicating that the formation of carbene carbon in PIL-imidaz is much less than that of P(triaz) in the presence of $NaBH_4$.

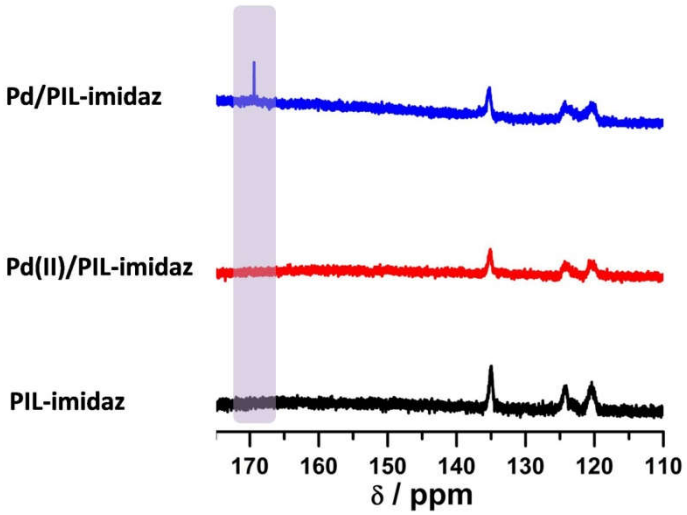

Figure S59. ^{13}C NMR spectra of PIL-imidaz, Pd(II)/PIL-imidaz and Pd/PIL-imidaz in CD_2Cl_2 and CH_3OH mixture (volume ratio = 2:1). In comparison to the PIL-imidaz, only a weak peak at 169.6 ppm appeared in Pd/PIL-imidaz (shown in violet rectangle). This phenomenon indicates that the PIL-imidaz is less efficient to generate polycarbene to control cluster formation in compared to P(triaz) after treated by $NaBH_4$. This is also consistent with the observation in the TEM image of non-uniform distribution of particles of Pd/PIL-imidaz (Figure S57).

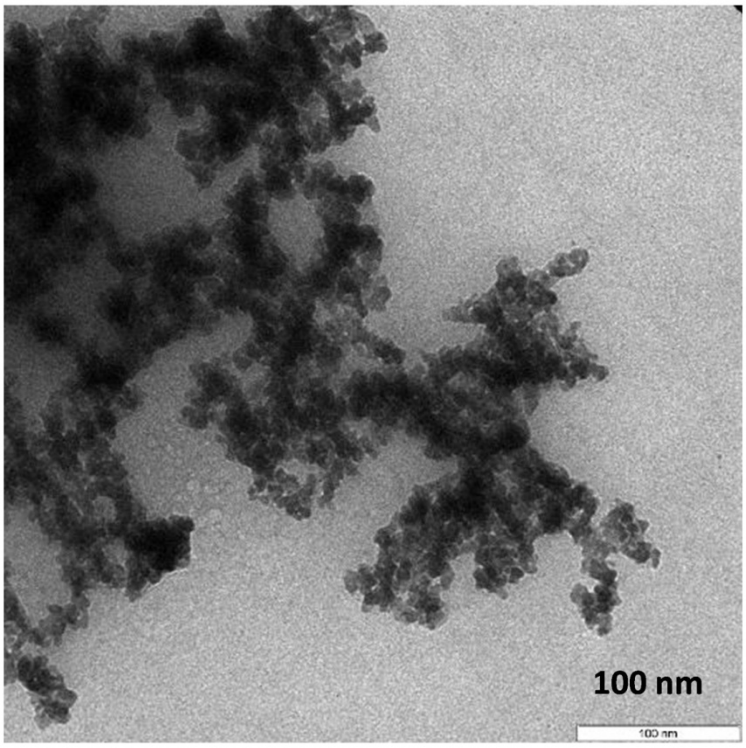

Figure S60. Bright field (BF) TEM image of the Pd/(triazolium monomer) formed by using triazolium monomer as stabilizer.

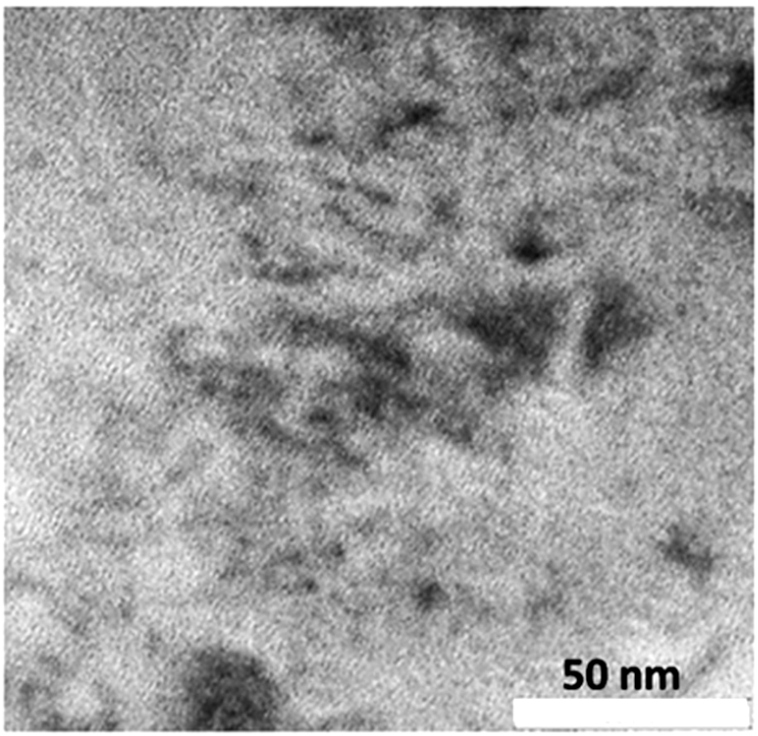

Figure S61. The TEM images of the Ag/P(triaz) nanoparticles prepared by using UV light radiation as reducing source.

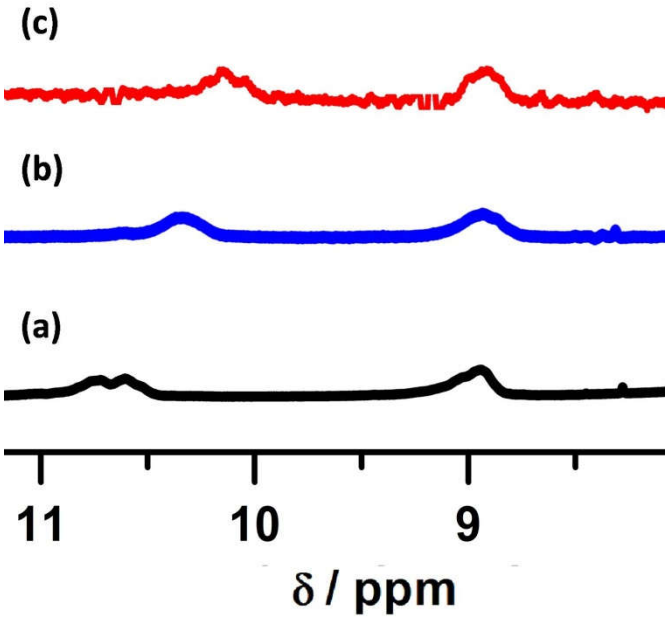

Figure S62. The ^{1}H NMR spectra of (a) P(triaz), (b) Ag(I)/P(triaz) and (c) Ag(I)/P(triaz) after reduction by UV irradiation in a CD_2Cl_2 and CH_3OH mixture (volume ratio = 2:1). The proton at C5 position has little-to-no change in its intensity, indicating that no detectable amount of carbenes was generated in this photoreduction process.

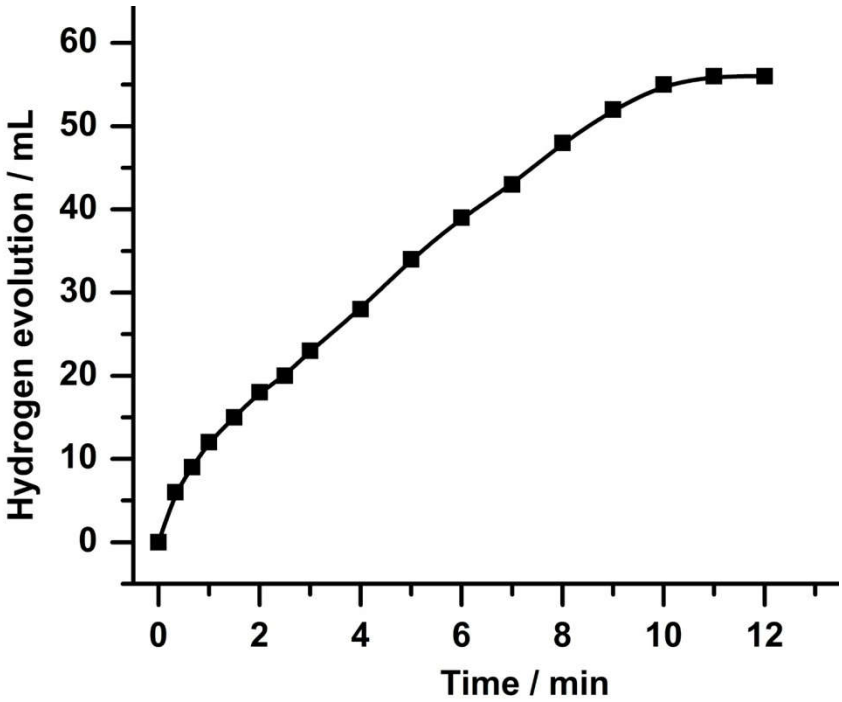

Figure S63. Time course plot of H_2 generation for the methanolysis of AB over the commercial Pd/C catalyst at 298 K (Pd/AB =0.01) (TOF: 22.4 min^{-1}).

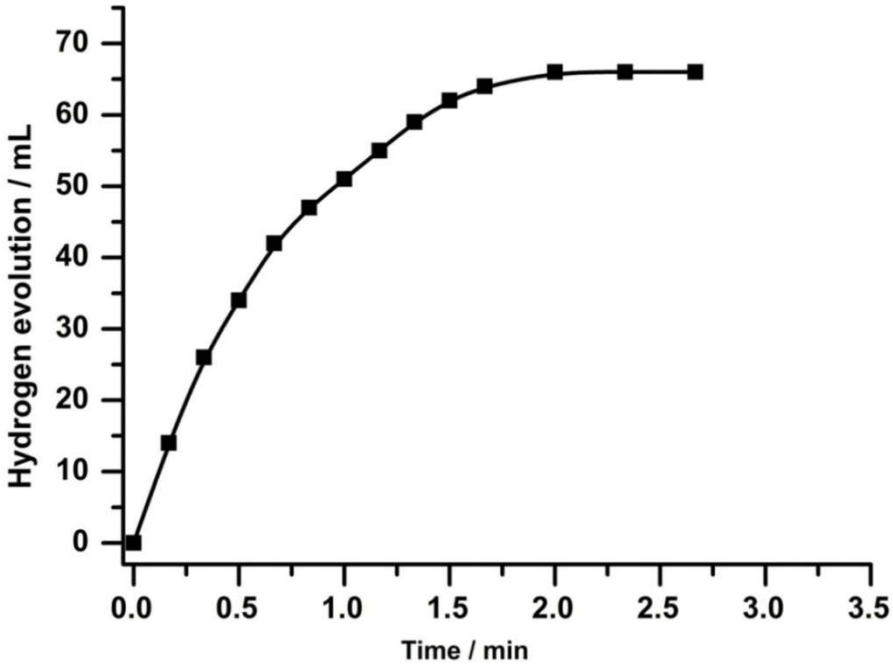

Figure S64. Time course plot of H_2 generation for the methanolysis of AB over the Rh/ triazolium monomer catalyst at 298 K (Rh/AB =0.01).

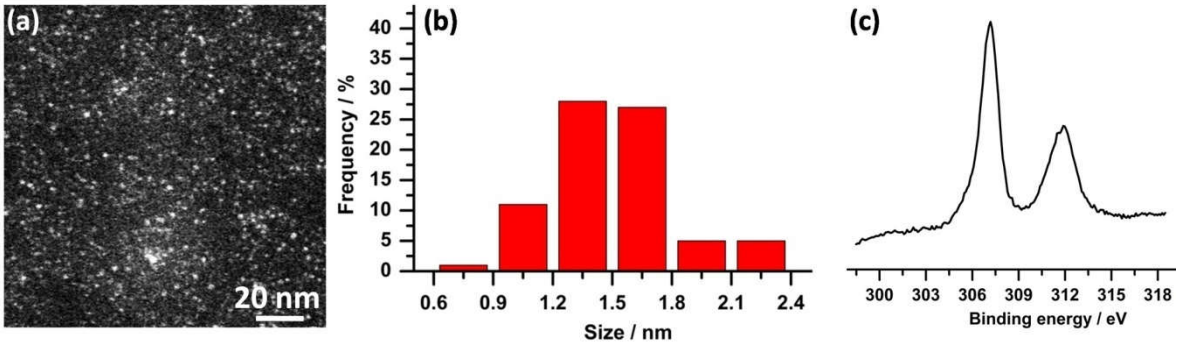

Figure S65. (a) HAADF-STEM image of Rh/PAMAM-OH catalyst and (b) the corresponding size distribution histogram of Rh clusters. (c) The XPS spectrum of Rh cluster.

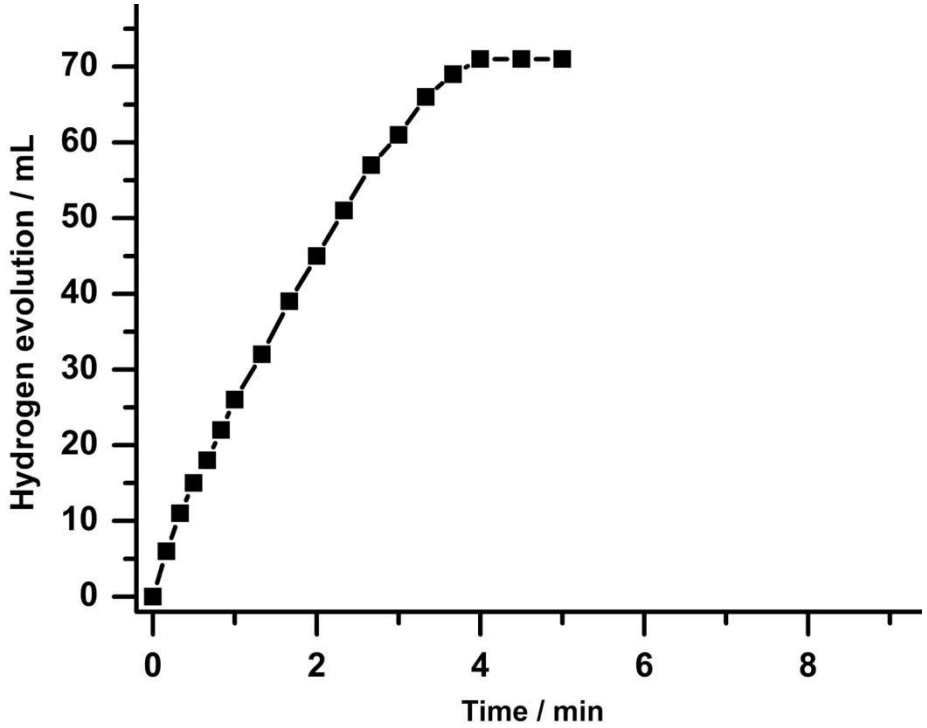

Figure S66. Time course plot of H_2 generation for the methanolysis of AB over the Rh/PAMAM-OH catalyst at 298 K (Rh/AB =0.01).

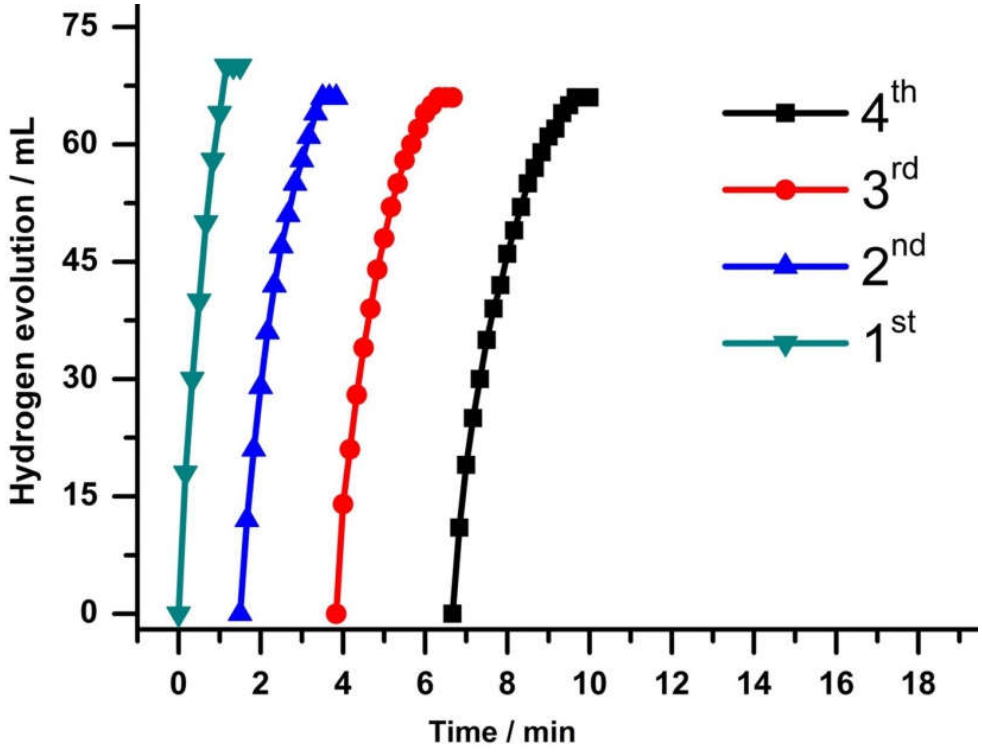

Figure S67. Durability test for AB methanolysis reaction over Rh/P(triaz) catalyst at 298 K (Rh/AB = 0.01).

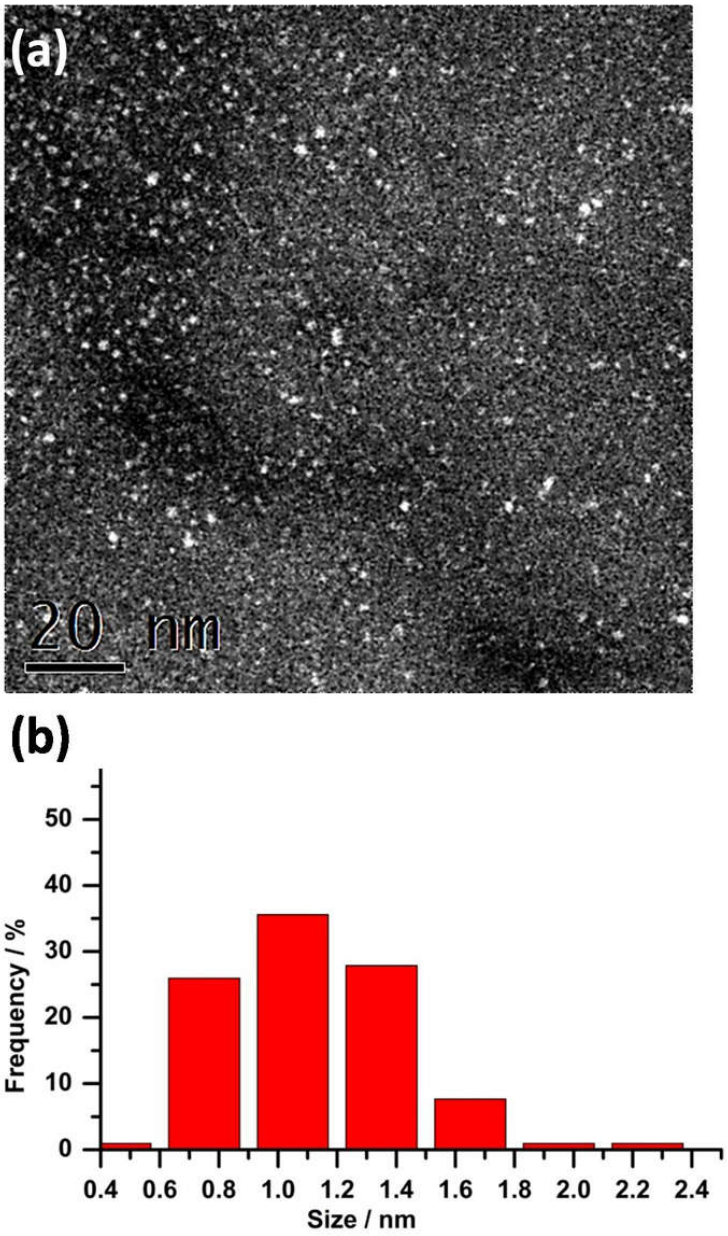

Figure S68. (a) STEM-HADDF image and (b) the size distribution histogram of Rh cluster of the as-synthesized Rh/P(triaz) catalyst before AB methanolysis reaction.

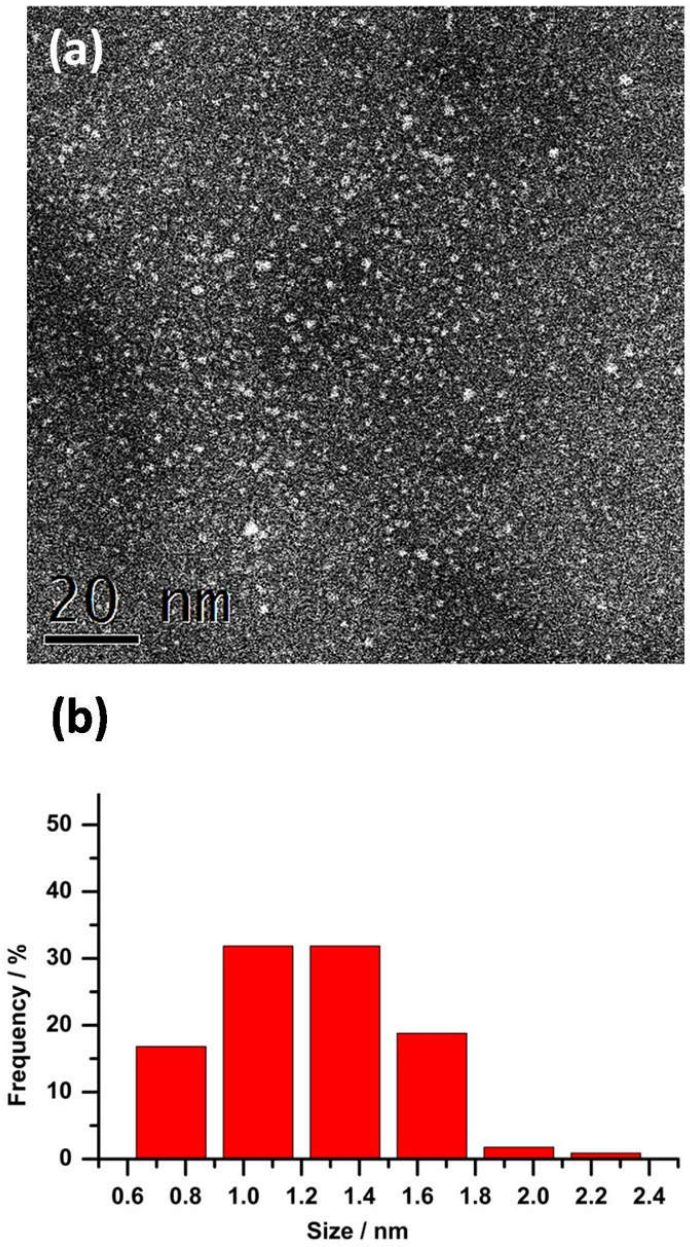

Figure S69. (a) STEM-HADDF image and (b) the size distribution histogram of Rh cluster of the Rh/P(triaz) catalyst after AB methanolysis reaction (Rh/AB = 0.01).

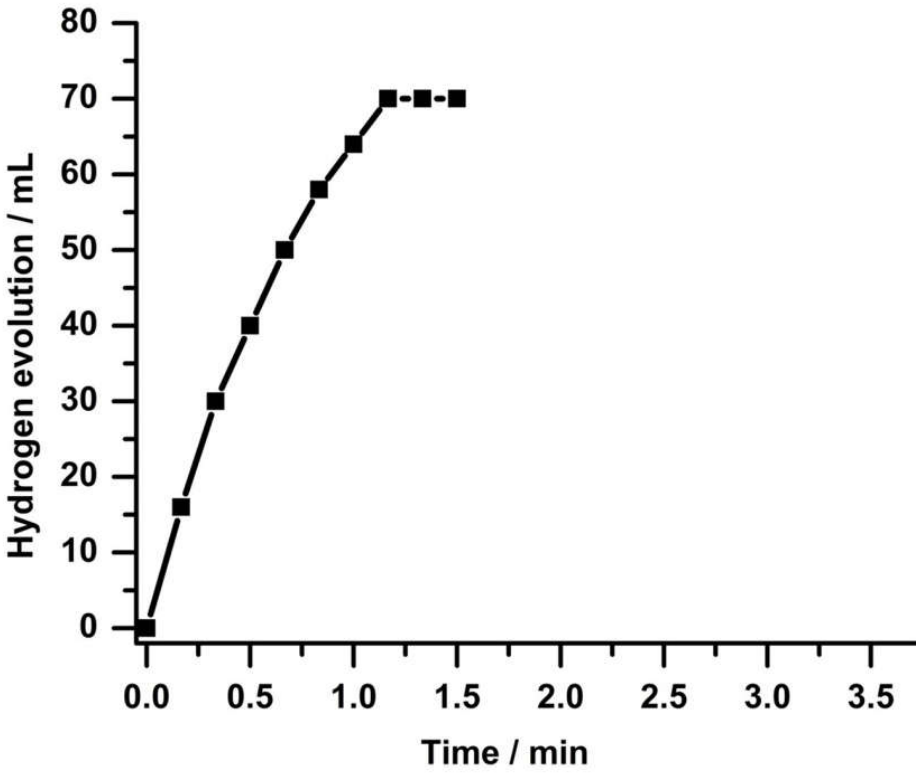

Figure S70. Time course plot of H_2 generation for the methanolysis of AB over the recycling catalyst generated by redissolving the N_2-dried Rh/P(triaz) catalyst (Rh/AB = 0.01) in a dichloromethane and methanol mixture (volume ratio = 2:1).

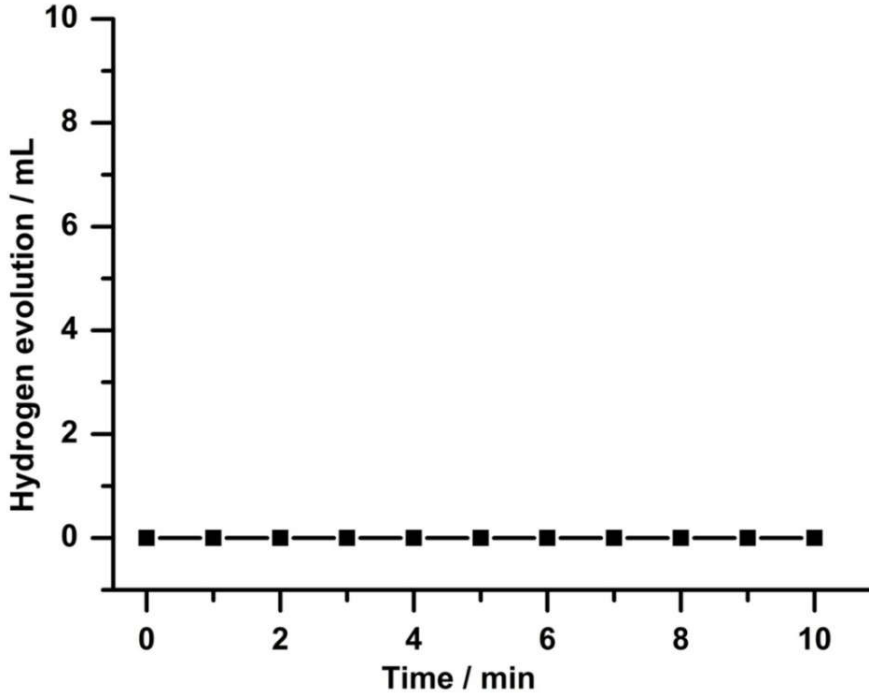

Figure S71. Time course plot of H_2 generation for the methanolysis of AB over only P(triaz).

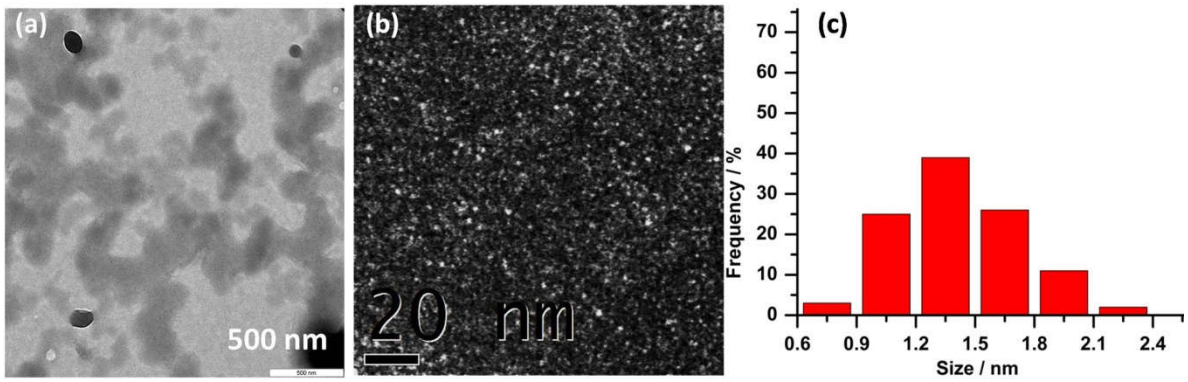

Figure S72. (a) TEM image of P(triaz) and (b) HAADF-STEM image of Rh/P(triaz) dried from their methanol solutions. (c) The corresponding size distribution histogram of Rh clusters (1.4 ± 0.3 nm).

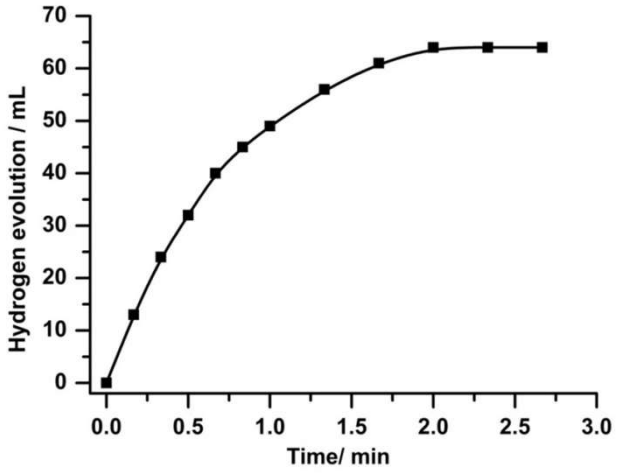

Figure S73. Time course plot of H_2 generation for the methanolysis of AB over the Rh/P(triaz) catalyst (Rh/AB = 0.01) in methanol.

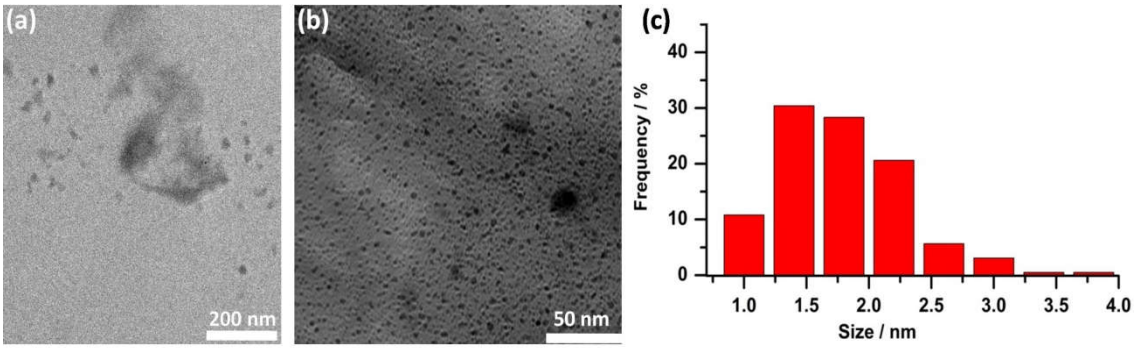

Figure S74. (a) TEM image of PIL-butyl and (b) Rh/PIL-butyl dried from their in dichloromethane and methanol mixture (volume ratio = 2:1). (c) The corresponding size distribution histogram of Rh clusters (1.8 ± 0.4 nm).

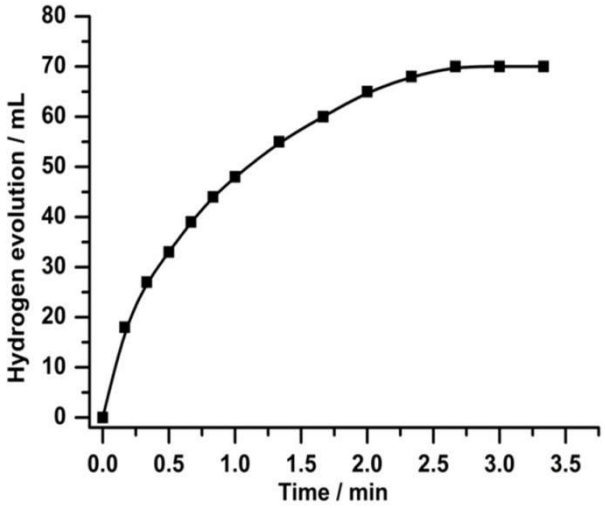

Figure S75. Time course plot of H_2 generation for the methanolysis of AB over the Rh/PIL-butyl catalyst (Rh/AB = 0.01) in a dichloromethane and methanol mixture (volume ratio = 2:1).

Table S1. The calculated molar ratio of carbene/metal in the meetal/P(triaz) products.

	Amount of metal (mmol)[a]	Amount of carbene generated in P(triazo) (mmol)[b]	Carbene/metal molar ratio
Ru	0.01	0.0111	1.11
Rh	0.0049	0.0098	2.00
Pd	0.0047	0.0054	1.15
Ag	0.0046	0.0046	1.00
Pt	0.0026	0.0047	1.81
Au	0.0025	0.0051	2.04

[a] The metal content in each specie is 0.5 mg except 1 mg for Ru.

[b] The amount of carbene is calculated by integrating the C-5 proton signal in the ^{1}H NMR spectra in Figure S38 and comparing this value with native P(triaz). The origin amount of P(triaz) is 5 mg for each metal specie.